RESEARCH ARTICLE

WILEY

Fragility and vulnerability analysis of deteriorating ordinary bridges using simulated ground-motion sequences

Kenneth Otárola[1] ⓘ | Jawad Fayaz[2,3] ⓘ | Carmine Galasso[1,2] ⓘ

[1]Department of Science, Technology, and Society, Scuola Universitaria Superiore (IUSS) Pavia, Pavia, Italy

[2]Department of Civil, Environmental, and Geomatic Engineering, University College London, London, UK

[3]School of Computing, Engineering, and Digital Technologies, Teesside University, Teesside, UK

Correspondence
Carmine Galasso, Department of Civil, Environmental, and Geomatic Engineering, University College London, London, UK.
Email: c.galasso@ucl.ac.uk

Abstract

Highway bridges are critical components of the lifeline transport infrastructure in urban areas. They are designed with the expectation of not sustaining significant structural/non-structural damage after major earthquake-induced ground shaking. However, in the current structural performance-based assessment practice, the effects of a pre-damaged state during ground-motion sequences are often neglected. Additionally, environmentally induced deterioration mechanisms (e.g., steel rebar corrosion) may exacerbate the consequences of such ground-motion sequences on the seismic structural performance during the bridge design lifetime; yet such effects are commonly overlooked. This study proposes a computational methodology to derive state-dependent fragility and vulnerability relationships (i.e., explicitly depending on the damage state achieved by the bridge structure during a first shock) for bridge structures subjected to chloride-induced corrosion deterioration and ground-motion sequences. The methodology is demonstrated for a case-study ordinary bridge structure (representing a typical bridge vulnerability class in southern California) under seismic sequences assembled from the CyberShake 15.12 (hybrid) simulated ground-motion database. In the proposed approach, parameterised (i.e., dependent on the corrosion deterioration level) vector-valued probabilistic seismic demand models are developed for the bridge components (i.e., columns and shear keys). These models, calibrated through sequential cloud-based nonlinear time-history analyses, relate the dissipated hysteretic energy in the ground-motion sequence to a deformation-based engineering demand parameter induced by the first shock and a ground-motion intensity measure of the second shock for a given corrosion deterioration level. Fragility relationships are first derived for a single ground motion at the component-level; state-dependent fragility relationships are then derived by considering the additional damage induced by a second ground motion within the simulated sequence (structure-specific damage states are considered). Furthermore, a component-based simulation approach accounting for the correlations across the components' response is utilised to

derive fragility relationships at the system level (i.e., for the bridge structure). Finally, appropriate damage-to-loss models for ordinary bridges are used to derive state-dependent vulnerability relationships. The results demonstrate the significant impact of earthquake-induced ground-motion sequences and environmentally-induced corrosion deterioration, emphasising the necessity of accounting for this multi-hazard threat in the structural performance-based assessment of bridges. Relative variations up to 120% can be found in the system-level state-dependent fragility median values comparing the results for the bridge in pristine and deteriorated conditions.

1 | INTRODUCTION

Highway bridges form an essential part of the lifeline transport infrastructure in major urban areas. Their satisfactory structural and non-structural performance (e.g., their safety) is vital to ensure adequate recovery after significant disastrous events (i.e., their resilience), such as those due to significant earthquake-induced ground shaking. Therefore, bridges are designed with the expectation of not sustaining significant damage and maintaining their functionality after major earthquakes and during their service life.[1] Current procedures to assess the seismic structural performance of bridges rely on performing several nonlinear structural analyses, each considering a single earthquake excitation. The analysis results are then statistically processed to derive the distribution of structural response and resulting damage/loss estimates. However, a bridge located in a seismically active region typically undergoes multiple ground-motion sequences (including multiple mainshocks, mainshocks triggering additional earthquakes on nearby fault segments, mainshock–aftershock and aftershock–aftershock sequences) during its design lifetime. Thereby, a bridge structure can frequently be in a pre-damaged state (due to previous ground motion(s)) while undergoing a seismic excitation. This series of back-to-back earthquake events can lead to severe structural/non-structural damage and unexpected seismic behaviour of the bridge (e.g.,[2,3]), as well as significant direct/indirect earthquake-induced losses. Additionally, while ground-motion sequences lead to intermittent shocks for a structure, deteriorating effects (e.g., steel rebar corrosion) constitute a continuous mechanism of environmentally-induced damage accumulation (e.g.,[4,5]). It has been confirmed that a substantial percentage of bridges across the globe show visible signs of ageing and deterioration, especially apparent when they approach the end of their service life (e.g.,[6,7]). Therefore, simultaneous consideration of earthquake sequences and environmentally-induced deterioration in seismic-prone regions is critical for risk-informed decision making on potential mitigation strategies for vulnerable bridges.

In the last decade, several studies attempted to account for ground-motion sequences in structural response analysis and damage/loss estimations of buildings and lifeline infrastructure systems (e.g.,[8,9]). Those studies were often driven by catastrophic events, such as the 2010–2011 Christchurch seismic sequence, which resulted in 185 human casualties and nearly $15 billion in financial losses (e.g.,[10]). However, few studies jointly consider repeated seismic events and environmental deteriorating effects in the structural performance-based assessment of structures. Such considerations are essential for bridges exposed to environmental processes that induce multiple forms of deterioration (e.g.,[11,12]). In particular, steel rebar corrosion has gained significant research and practical interest in the recent past concerning bridge structural performance under service loads or during a single seismic excitation. Some studies have investigated the issue of sequential ground motions adopting both single-degree-of-freedom systems (e.g.,[13,14]) and multi-degree-of-freedom systems (e.g.,[15,16]), concluding that the deformation response is increased under multiple consecutive ground motions leading to a significant reduction of structural capacity. Such findings are highly important from a perspective of life-cycle analysis since the assumption of structural damage being repaired to a pristine condition before subsequent ground motions (e.g.,[17]) is not always valid. The previous consideration is especially true when: (a) the level of damage resulting in structural deterioration after a seismic event is not visually significant to prompt repair/retrofit actions; (b) the economic constraints

render repair/retrofit or structural upgrade infeasible after every earthquake event; and (c) the time between consecutive earthquake events is relatively short for initiating repair/retrofit operations.

The importance of considering primary (i.e., the propagation phase) and secondary effects of environmentally-induced corrosion deterioration in material properties for lifetime structural response and damage/loss analysis of bridges have been addressed by several studies (e.g.,[18,19]). Those studies highlight the potential underestimation of seismic life-cycle costs when not accounting for time-dependent bridge deterioration (e.g.,[20,21]). Amongst the various types of steel rebar corrosion that bridges are likely to experience when exposed to environmental conditions, chloride-induced corrosion is of special interest from the structural performance viewpoint.[22] Depending on the severity of the environmental exposure, this deterioration mechanism may potentially lead to significant reductions in the structural capacity of critical bridge components (e.g.,[23,24]). However, to the best of the authors' knowledge, no studies developed state-dependent fragility relationships (i.e., fragility relationships that explicitly depend on the damage state achieved by the bridge structure during a first shock) for seismically pre-damaged bridge structures considering different damage states (DSs) under chloride-induced corrosion attacks. Additionally, no attention is given to developing state-dependent vulnerability relationships (i.e., the probability of various loss levels as a function of a hazard intensity measure (IM) and the damage state achieved by the structure during a first shock) for the same settings mentioned above. Such vulnerability relationships can be practically implemented for applications such as bridge-specific and bridge-portfolio loss assessment (e.g.,[25,26]). This study addresses the above gaps and derives state-dependent fragility and vulnerability relationships under earthquake-induced ground-motion sequences and chloride-induced corrosion deterioration.

Apart from the difficulties in assessing the seismic structural performance of deteriorating bridges under the effects of ground-motion sequences, the scarcity of suitable real (i.e., as-recorded) ground motions for conditions not well-represented in recorded databases (e.g.,[27]) makes the utilisation of alternative options inevitable. This is especially evident in earthquake-prone regions (e.g., southern California), where the pseudo-spectral accelerations (SAs) for hazard levels of interest are often relatively large.[28] To address the above issue, physics-based and/or stochastic/semi-stochastic simulated ground motions (e.g.,[29,30]) capturing complex source features and site effects represent a convenient supplement.[31] One of the major noteworthy efforts in this field has been made by the southern California Earthquake Centre (SCEC) and the United States Geological Survey (USGS). In particular, CyberShake 15.12[32] relies on the earthquake rupture information from the Uniform California Earthquake Rupture Forecast Version 2 (UCERF2)[33] for the active faults (including background seismicity) and provides ground motions for ~900 sites in Southern California using three-dimensional hybrid simulation models (i.e., physics-based for low frequencies ≤1 Hz and semi-stochastic for high frequencies >1 Hz). Many subsequent studies performed engineering validation exercises, demonstrating that the resulting simulations are highly comparable to recorded ground motions for performance-based assessment of structures such as ordinary bridges, buildings, single-degree-of-freedom systems, etc. (e.g.,[34–36]). Hence, in this study, CyberShake 15.12 ground-motion database is used to perform ground-motion record selection to assemble ground-motion sequences.

Currently, there is significant consensus that structural response is not only dependent on the bridge's characteristics but also on the seismological features (e.g., rupture mechanism, earthquake magnitude, source-to-site distance, soil type, etc.) and the ground-motion amplitude, frequency-content and duration consistent with the seismic hazard of a considered site (e.g.,[37]). In this study, a random sampling approach is utilised to assemble simulated ground-motion sequences directly from the CyberShake 15.12 ground-motion database (using the available rate of occurrences for the rupture variations) to derive state-dependent fragility and vulnerability relationships that can be used under multiple ground motions that could occur in the form of typical mainshocks, aftershocks, or triggered earthquake events. Site-specific hazard consistency (e.g.,[38,39]) is not explicitly addressed in the ground-motion record selection executed, potentially introducing some bias in the results attained. Nevertheless, the considered selection approach is coherent with the adopted nonlinear analysis procedure (i.e., cloud-based analysis) that relies on selecting unscaled ground motions covering a wide range of intensity levels. The previous approach is deemed appropriate for applications related to bridge-portfolio loss assessment rather than those related to site- and bridge-specific loss assessment. Additionally, the conditioning IM selected for this study (i.e., average pseudo-spectral acceleration, $avgSA$) has demonstrated being more sufficient and efficient than other typical IMs (e.g.,[40,41]), meaning that fragility/vulnerability analysis outcomes are going to be less sensitive to seismological features and ground-motion characteristics (e.g., spectral shape), which are explicitly accounted for when executing a site-specific, hazard-consistent ground-motion record selection.
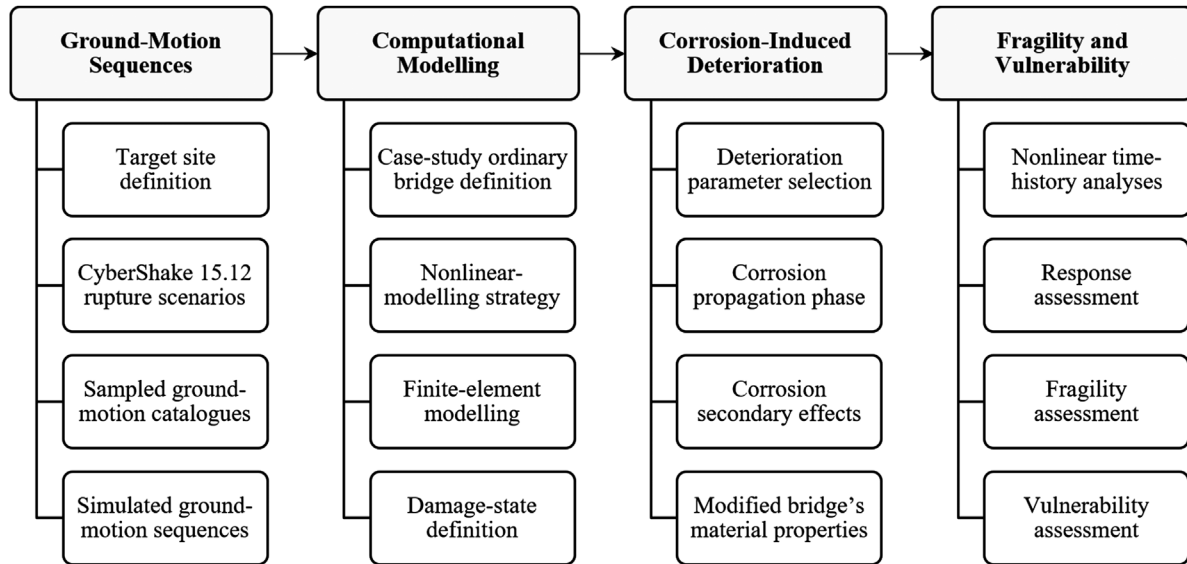
FIGURE 1 Adopted methodology for fragility and vulnerability analysis of deteriorating ordinary bridges under simulated ground-motion sequences

Based on this background and remarks, this paper presents a computational methodology to carefully select (hybrid) simulated ground motions (using catalogues representing realisations of 100-year seismicity) to assemble seismic sequences which are utilised to develop state-dependent fragility and vulnerability relationships for deteriorating reinforced concrete (RC) ordinary bridges. The methodology is illustrated using a real case-study ordinary bridge under the effects of ground-motion sequences assembled through a plain Monte-Carlo sampling approach from the CyberShake 15.12 ground-motion database. Specifically, parameterised (i.e., dependent on a corrosion deterioration level) vector-valued probabilistic seismic demand models (PSDMs) are derived for each bridge critical component (i.e., columns and shear keys). The developed models relate the dissipated hysteretic energy in the sequence to a deformation-based engineering demand parameter (EDP) induced by the first shock and a ground-motion IM of the second shock, calibrated through sequential cloud-based nonlinear time-history analyses (NLTHAs) for a given corrosion deterioration level. The fragility relationships for the bridge components are first derived for a single ground motion; state-dependent fragility relationships are then derived by considering the additional damage induced by a second ground motion within the simulated seismic sequence. Moreover, a component-based simulation approach accounting for the correlations across the component response through a joint PSDM is utilised to derive fragility relationships for the bridge structure. Finally, appropriate damage-to-loss models for ordinary bridges are used to propose state-dependent vulnerability relationships.

This paper is organised as follows. Section 2 describes the methodology for developing state-dependent fragility and vulnerability relationships, including the effects of ground-motion sequences and chloride-induced corrosion deterioration. Section 3 presents the main findings from the analyses, which are discussed based on a thorough examination of the results. Lastly, Section 4 outlines the main conclusions of this study and its implementation.

2 | METHODOLOGY

An actual symmetric double-span box-girder seat-type bridge (denoted as bridge B in Fayaz et al.[42]) is selected as a study case; nevertheless, the proposed methodology can be implemented on any bridge with a ductile response on its structural components. The following details apply to such bridge: deck width: 23 m; number of spans: two; span lengths: 45.7 m; number of columns: two; columns radius: 0.85 m; columns height: 6.70 m. The considered bridge represents a typical vulnerability class in southern California (La Veta Avenue, Orange, CA, USA). The adopted methodology is illustrated in Figure 1 and consists of four main phases. First, simulated ground-motion sequences composed of two consecutive (hybrid) simulated ground motions are assembled from the CyberShake 15.12 ground-motion database. Secondly, a computational three-dimensional finite-element model of the case-study ordinary bridge is built, capable of accounting for

deteriorating effects (specifically, due to steel rebar corrosion) in the various material properties. Thirdly, the bridge structure's material properties are modified to account for chloride-induced corrosion propagation and its secondary effects. Fourth and finally, state-dependent fragility and vulnerability relationships are derived at the bridge-component (i.e., columns and shear keys) and the bridge-system (i.e., structure) level. Details related to this methodology are described in the subsequent subsections of this study.
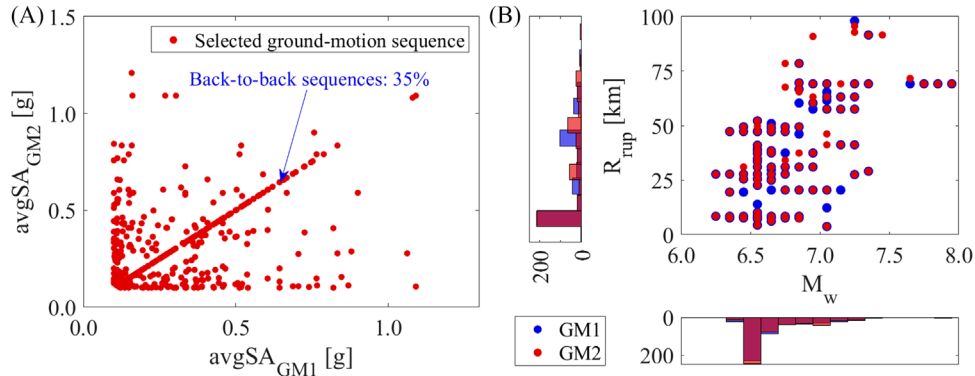
2.1 | Ground-motion sequences

Due to the low availability in empirical databases of earthquake sequences characterised by strong ground motions of engineering relevance, the observations of significant damage increase due to sequential earthquake excitations are limited. In turn, this does not allow the derivation of statistically robust fragility and vulnerability relationships conditioned on an initial DS due to an initial shock. The hybrid ground motions simulated for CyberShake 15.12 are utilised in this study to overcome this challenge. In CyberShake 15.12, deterministic physics-based models are utilised to simulate ground-motion waveforms for low frequencies ($\leq$1 Hz)[29]; the resulting simulations are then augmented with semi-stochastic high-frequency ($>$1 Hz) simulations generated using the Graves and Pitarka method.[32] This simulation approach is utilised alongside the source/fault rupture information from UCERF2 to obtain ground motions for ∼900 site grid in the southern California region. UCERF2 provides a list of potential ruptures for active seismic faults in California, along with their annual probabilities of occurrence. Also, it introduces a suite of variations in hypocentre locations and slip distributions to account for the natural variability in rupture characteristics. The ruptures are assumed to be independent, and all the hypocentral variations are assumed to be equally likely for each rupture.[34] It should be noted here that CyberShake 15.12 does not use UCERF2 directly, and additional modifications and constraints are incorporated in the earthquake rupture forecast model to simulate the hybrid ground motions. This results in a total of ∼415,000 simulated ground-motion waveforms, each associated with a rupture variation for each site. In this study, among the ∼900 sites available within the CyberShake 15.12 ground-motion database, simulations are obtained for Los Angeles Downtown (LADT) (Latitude: 34.052; Longitude: −118.257; shear-wave velocity averaged over the top-most 30 m of soil: 358.60 m/s; depth where shear-wave velocity is equal to 2.5 km/s: 2.08 km; e.g.,[34]) that arise from seismic sources within 100 km of the site. The seed ground-motion records used in this study are selected for LADT for convenience (i.e., CyberShake simulations are readily available, and moderate-to-high ground motions characterise the site, resulting in nonlinear structural responses of the case-study bridge). Nevertheless, the same ground motions can represent a broader area (e.g., the Greater Los Angeles Area or even different regions) in terms of their seismological features (e.g., causal parameters, such as magnitude and source-to-site distance) and ground-motion characteristics. It is worth mentioning that a ground-motion subset from the CyberShake 15.12 study representative of the Greater Los Angeles area is available and ready to be used, with ground motions selected based on disaggregation of seismic hazard.[35]

Using the available rate of occurrences for the rupture variations, the simulated ground motions for LADT are randomly sampled to obtain subset ground motions to assemble catalogues representing realisations of 100-year seismicity (i.e., a typical bridge design lifetime according to Caltrans[1]). In total, 50,000 realisations are independently simulated through plain Monte-Carlo sampling. It is worth noting that the earthquakes from a rupture are assumed to follow a homogenous Poisson (time-independent) process in CyberShake 15.12; thus, the interarrival time between ground motions is randomly sampled following an exponential distribution. Furthermore, it is worth noting that only the horizontal components of the simulated ground motions are utilised in this study. It has been demonstrated in the literature that significant vertical ground motions can exacerbate the damage observed in a bridge's superstructure (mainly) and substructure, especially during near-fault earthquake events that can generate high vertical accelerations due to pulse-like ground motions (e.g.,[43]). However, the adopted case-study bridge structure is not expected to be susceptible to vertical ground-motion effects (e.g., columns' buckling), given its modern seismic-resistant structural detailing.[44] Hence, the ground motions' vertical component is neglected for simplicity without expecting to impact the generality of the results.

The considered approach leads to, on average, nine mainshock-induced ground motions for each realisation, presenting a wide range of ground-motion characteristics from which ground-motion sequences are then assembled using consecutive (hybrid) simulated ground motions. Finally, the 500 ground-motion sequences (i.e., a first ground motion, GM1; followed by a second ground motion, GM2; consequently, 1,000 individual ground motions in total) with higher $RotD50avgSA$ (denoted herein as $avgSA$ for brevity) in both shocks (Figure 2A) and lower interarrival time, are arbitrarily selected (with a minimum threshold of 0.1 g). Note that in the previous IM syntaxis, Rot indicated the rotation of the ground-motion components, D indicates the period dependency, and 50 indicates the percentile value used to com-

FIGURE 2 Selected ground-motion sequence metadata: (A) scatter of $avgSA_{GM1}$ versus $avgSA_{GM2}$, and percentage of back-to-back ground-motion sequences (i.e., sequences assembled with two identical mainshocks); (B) scatter and marginal histogram of M_w versus R_{rup} for both, GM1 and GM2 of each ground-motion sequence

pute the demand. The previous IM is estimated as the geometrical mean of 12 equally-spaced $RotD50$ pseudo-acceleration spectral ordinates[45] within the range $[0.5T_3, 1.5T_1]$, where T_1 is the dominant structural period in the longitudinal direction (i.e., the fundamental structural period of the considered structure/bridge) and T_3 is the dominant structural period in the transversal direction.[46] In Figure 2B, a scatter plot of moment magnitude (M_w) and closest distance to the rupture (R_{rup}) for the selected ground motions within the sequences are shown ($avgSA_{GM1}$ and $avgSA_{GM2}$ are the $avgSA$s related to GM1 and GM2, respectively). Note that to build the ground-motion sequences the two ground-motion waveforms are appended with a padding of zeros equivalent to the length of $20T_1$. This allows the bridge structure to attain its steady-state response between and after the last ground motion within the assembled sequence. The first three modal structural periods belonging to the case-study ordinary bridge structure are $T_1 = 0.83$ s, $T_2 = 0.44$ s, and $T_3 = 0.37$ s, respectively.

It is worth mentioning again that the proposed sequences are assembled by randomly sampling the ground motions using the available rate of occurrences from the CyberShake 15.12 rupture variations following the Poisson assumption using mainshock-induced ground motions only, without considering the: (a) dependency of mainshocks on specific fault segments since the probability of having a similar magnitude earthquake might be lower than average after a segment rupturing earthquake; (b) interaction between adjacent faults since an earthquake on one fault may delay or trigger the rupture occurrence of other events on the surrounding faults; (c) the spatial and temporal clustering of foreshocks and aftershocks (i.e., smaller-magnitude earthquakes prior and after a mainshock, correspondingly) (e.g.,[47]). Based on these observations, bias may be introduced in the fragility/vulnerability analysis results by using mainshock-induced ground motions without accounting for the corresponding seismological features and ground-motion characteristics of each earthquake-event type (i.e., mainshock, aftershock and triggered earthquake) originating typical ground-motion sequences. However, the employed nonlinear analysis procedure (i.e., sequential cloud analysis) and the use of a highly sufficient and efficient IM in this study should reduce any potential biases in the fragility/vulnerability model estimates (e.g.,[37]), as mentioned above. It is worth noting also that the CyberShake 15.12 ground-motion database is only available for California. However, any subset of real (i.e., as-recorded) ground motions can also be utilised to derive the state-dependent fragility and vulnerability relationships as later introduced, complying with the seismological features and ground-motion characteristics of the site (or region) of interest from empirical ground-motion databases (e.g.,[27]).

2.2 | Computational modelling

The case-study ordinary bridge's computational three-dimensional finite-element model is developed using the open-source software framework OpenSeesPy.[48] The model is developed to represent the geometry, boundary conditions, mass distribution, energy dissipation and the interaction among the structural components of the bridge structure. The components comprise seat-type abutments (which include an arrangement of nonlinear springs for shear keys, elastomeric bearing pads, soil backfill, and abutment piles), column bents (which include nonlinear fibre sectional models for columns and column foundational springs) and an elastic superstructure representing the box-girder deck. The bridge computational model was initially based on the ones presented by Omrani et al.[49]; however, their structural component models are upgraded, and associated modelling parameters are updated. Xiang et al.[50] showed that this model might reproduce a

closer structural response to what is recorded on instrumented bridges in California under various seismic settings compared with the models proposed by the Caltrans Seismic Design Criteria[1,51] (e.g.,[34]). It is worth mentioning that this model can account for deteriorating effects due to chloride-induced corrosion in the various material properties as appropriate.

Specifically, according to the Caltrans Seismic Design Criteria,[1] a bridge's superstructure is designed to remain elastic during significant earthquake-induced ground shaking. Hence, the superstructure is modelled with the *elasticBeamColumn* element using uncracked section properties. The superstructure's mass is distributed throughout the length of the deck, with each span's mass being distributed in ten intervals. The bridge columns are modelled with fibre-discretised cross-sections using the *forceBeamColumn* element, utilising the *HingeRadau* integration method. The confined concrete for the core is modelled using the *Concrete04* material, the unconfined concrete for the cover using the *Concrete01* material, and the steel rebars using the *ReinforcingSteel* material, including steel rebars' buckling and low-cycle fatigue behaviour. The plasticity in the columns is concentrated at two plastic hinges located at the opposite ends of the columns connected by a linear elastic element (i.e., a lumped-plasticity modeling strategy is employed). The shear and torsional behaviour of columns are modelled using an elastic *uniaxialMaterial* because shear failures are not expected, given the modern seismic-resistant detailing characterising the case-study bridge,[52] as mentioned before. Assuming an integral construction between the cap beam and the columns, the cap beam is modelled as a rigid bent using the *elasticBeamColumn* element with high torsional, in-plane and out-of-plane stiffnesses. The bases of the bridge structure are simulated as pinned connections. However, the flexibility of base connections arising from piles beneath is modelled explicitly by describing the translational behaviour of pile foundations using the *Elastic* material, although vertical movement is restricted. For the transverse direction of the abutments, shear keys are designed and modelled to behave in an isolated manner, as per the experimental results of Kottari.[53] Shear keys are modelled using the *Hysteretic* material. The model is defined with a trilinear backbone curve explaining the highly stiff elastic, hardening and softening parts of the hysteretic behaviour. The response of the abutment in the longitudinal direction is modelled by combining (a) abutment piles; (b) soil backfill; and (c) elastomeric bearing pads. The abutment model in the transversal direction comprises (a) abutment piles; (b) shear keys; and (c) elastomeric bearing pads. The piles of the abutments are modelled through a trilinear *Hysteretic* material with the backbone curve defined by Choi.[54] The soil backfill is modelled using the *HyperbolicGapMaterial* material with a generalised hyperbolic force-deformation backbone.[55] The piles underneath the abutment provide the active resistance of the abutment, while the combined action of the piles and soil backfill provides the passive resistance. The parameters described by Ramanathan[56] are used to model the elastomeric bearing pads using the *Steel01* material. The longitudinal behaviour of the abutment is modelled using five longitudinal abutment combo springs in parallel connected by a rigid beam. Conversely, the transverse behaviour is modelled using one combo spring at each abutment transversal end.

In Figure 3A, a schematic representation of the computational three-dimensional finite-element model for the case-study ordinary bridge is depicted. In Figure 3B–F, a schematic representation of the backbone curve (i.e., idealisation of the hysteretic response under a monotonic load) for the several components is shown. For further explanation of the model, the readers are referred to the work of Fayaz et al.[42]

2.3 | Corrosion-induced deterioration

Chloride-induced corrosion of steel rebar is one of the most significant environmental threats affecting the seismic structural performance of bridges worldwide (e.g.,[57]). Once the corrosion process initiates, a series of primary (i.e., propagation phase) and secondary effects can be observed in the affected RC components due to the extensive build-up of rust products (i.e., ferric oxide compounds). The propagation phase is related to the direct deterioration attained in the steel rebar (i.e., its cross-sectional area loss), while the secondary effects are related to the indirect deterioration of the steel rebar and the concrete properties (e.g., reduction of the ultimate strength and ultimate strain of the materials). In this study, the proposed state-dependent fragility and vulnerability relationships are not explicitly conditioned on time and an IM; instead, they are conditioned on a deterioration parameter (ψ) that is implicitly dependent on time and an IM. The herein selected ψ corresponds to the percentage of steel rebar area loss under uniform corrosion (e.g.,[58]), arbitrarily termed as corrosion deterioration level. The chloride-induced corrosion depends on the type of environmental exposure (i.e., on the aggressiveness of the corrosion rate of a particular site); therefore, unlike exposure-specific time-dependent fragility relationships, the relationships to be developed depending on ψ are more applicable and generic (i.e., practical) for different exposure scenarios and applications. It is worth noting that the corrosion rate (available for several environmental exposure scenarios based on the chloride concentration; e.g., marine atmospheric, marine sea-splash, deicing salt spray) provides the reduction in steel rebar radius per year, from where ψ can be obtained (implicitly depending on time). In
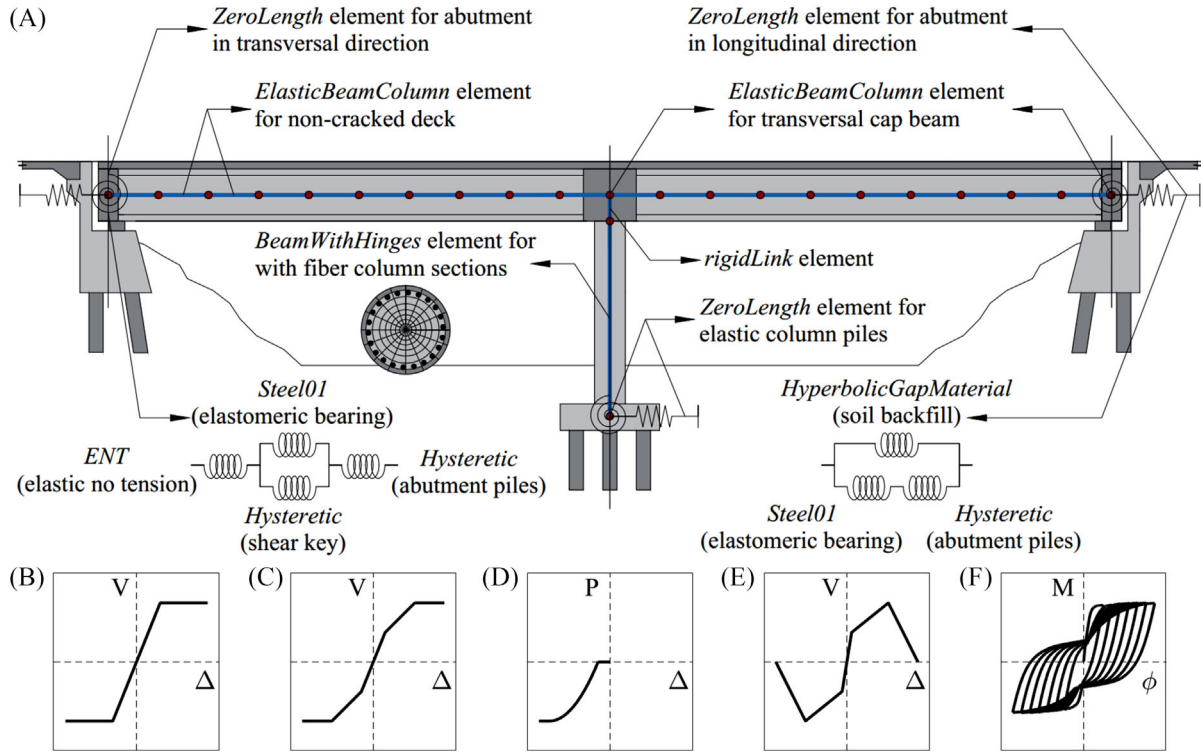
FIGURE 3 (A) Computational three-dimensional finite-element model scheme of the case-study ordinary bridge; (B) elastomeric bearing response; (C) abutment piles response; (D) soil backfill response; (E) shear key response; (F) column response. V stands for shear force, Δ stands for displacement, P stands for axial force, M stands for bending moment and ϕ stands for curvature

total, six equally spaced corrosion deterioration levels are considered in this study to perform the fragility and vulnerability analysis of the case-study ordinary bridge, ranging from $\psi = 0\%$ (i.e., pristine condition) up to $\psi = 25\%$ (for having realistic corrosion deterioration levels during the bridge design lifetime for usual environmental exposure scenarios; e.g., [22]). Further details about the corrosion-induced deterioration (i.e., the impact of corrosion on the material properties) are presented in the subsequent subsections.

2.3.1 | Corrosion propagation phase

The cross-sectional area loss of steel rebar in RC components starts after the corrosion initiation phase, during which chloride ions enter through the concrete cover and de-passivate the reinforcing steel. Following the initiation time, the early stages of propagation of the chloride-induced corrosion are characterised by the formation of small independent pits or cracks along the length of the steel rebar. Eventually, this phenomenon results in wider interconnected cracks leading to uniform (also known as generalised) corrosion (e.g.,[57,59]). However, in addition to the uniform area loss of steel rebar, localised corrosion (more severe) across multiple locations along the steel rebar leads to deep-pit formations (i.e., pitting sectional area loss). Past experimental investigations have reported that these cavities are often as large as four to eight times higher than the ones attained under uniform corrosion (i.e., uniform sectional area loss; e.g., [60]). The uniform corrosion model assumes a consistent loss of area around the circumference of the steel rebar during the bridge service life, estimated as in Equations (1) and (2), as a function of ψ. In these equations, $d(0)$ is the rebar diameter at pristine condition; $d(\psi)$ is the deteriorated rebar diameter under uniform corrosion; and $A_u(\psi)$ is the deteriorated rebar area under uniform corrosion. In contrast, the pitting corrosion model assumes an additional hemispherical area loss accompanying the loss attained due to uniform corrosion.[61] In Figure 4, a schematic representation of a single steel rebar subjected to uniform and pitting corrosion is shown for clarity. In this study, a probabilistic log-normal model $\gamma(\psi) \sim LN[\mu(\psi), \sigma(\psi)]$ accounting for this additional sectional area loss is adopted.[62] $\gamma(\psi)$ is the area pitting coefficient and is utilised to estimate $A_p(\psi)$, which is the deteriorated area under pitting corrosion as in Equation (3). The parameters $\mu(\psi)$ and $\sigma(\psi)$ are the distribution parameters (log-normal mean and standard deviation, respectively), as indicated by Kashani et al.[62] The expected
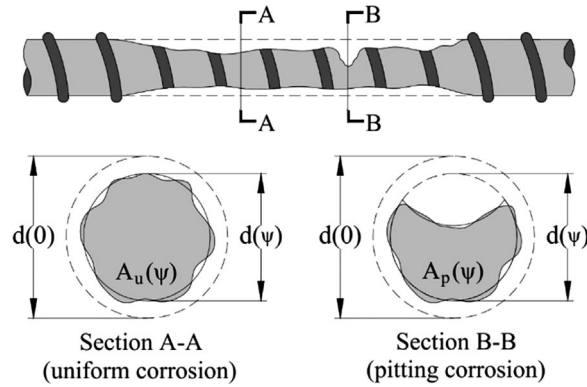
FIGURE 4 Uniform and pitting corrosion on a single steel rebar scheme (additional hemispherical cross-sectional area loss in the pitting corrosion case)

value of $\gamma(\psi)$ is utilised to account for pitting corrosion effects on the RC components (pitting corrosion is assumed to critically occur at the bridge column plastic hinge locations and bridge shear keys, given the nonlinear modelling strategy adopted). The spatial variability of this kind of corrosion along the steel rebar is not considered in this study (e.g.,[63]). The cross-sectional area loss is assumed to occur simultaneously in both bridge's columns and shear keys. Given the previous assumptions, it is worth noting that pitting corrosion is a spatio-temporal process. Specifically, this study considers the temporal dimension implicitly by using ψ, while the spatial one is neglected given the high uncertainty associated with the locations of the pits along the steel rebars; avoiding, in turn, the potential high computational burden. This aspect might lead to overestimating the fragility/vulnerability estimates of the structural components (e.g.,[64]). Moreover, corrosion deterioration levels are assumed to be perfectly correlated across the bridge structure since its components are similarly exposed to chlorides; however, this may result in highly correlated damage between these. This aspect can only be corroborated with accurate field test information from bridge monitoring of different structural components, helping in understanding and utilising uncorrelated or partially correlated corrosion data.

$$d\,(\psi) = \frac{d\,(0)}{10}\,\sqrt{100 - \psi} \tag{1}$$

$$A_u\,(\psi) = \frac{\pi}{4}\,[d\,(\psi)]^2 \tag{2}$$

$$A_p\,(\psi) = \gamma\,(\psi)\,A_u\,(\psi) \tag{3}$$

2.3.2 | Corrosion secondary effects

Along with uniform or pitting cross-sectional area loss of steel rebar, corrosion-based deterioration of RC components displays various secondary effects. The rust products occupy more volume than the original steel; consequently, the expanding volume of the corroding steel rebar leads to the formation of micro-cracks in the concrete cover, resulting in loss of compressive strength. The merge of these cracks leads to complete cracking and eventual spalling of the component concrete cover. The reduction in cover concrete strength can be estimated using Equation (4) (e.g.,[65]). In this equation, $f'_{cv}(0)$ is the compressive strength of cover concrete for the pristine column; κ depends on the steel rebar diameter and roughness (assumed to be 0.1 according to Vecchio and Collins[66]); ε_{cv} is the concrete compressive strain corresponding to the peak stress $f'_{cv}(0)$; and $\varepsilon^*(\psi)$ represents the average tensile strain in the transverse direction leading to the formation of microcracks due to corrosion estimated using Equation (5).[67] In this equation, v_{rs} is the ratio of volumetric expansion of rust products with respect to the volume of uncorroded steel rebar (assumed to be 2.0 based on Molina et al.[67]); $r_{rs}(\psi)$ is the depth of corrosion attack or reduction in steel rebar radius and at individual deep-pit locations; n_{bars} is the number of corroding steel rebars across the column section (all the reinforcing steel in the columns is assumed to be corroded);

and d_{col} is the diameter of the column in pristine condition.

$$f'_{cv} (v) = \frac{f'_{cv} (0)}{1 + \kappa \frac{\varepsilon^*(\psi)}{\varepsilon_{cv}}} \tag{4}$$

$$\varepsilon^* (t) = \frac{4\pi (v_{rs} - 1) r_{rs} (\psi) n_{bars}}{d_{col}} \tag{5}$$

The cross-sectional area loss of the steel rebar in transverse column ties may reduce the confined-core concrete strength. The confined concrete strength of the core is estimated using the theoretical stress–strain model proposed by Mander et al.[68] as in Equation (6). In this equation, $f'_{co}(\psi)$ is the deteriorated compressive strength of confined-core concrete after corrosion; f'_c is the compressive strength of unconfined-core concrete before corrosion; and $f_l(\psi)$ is the deteriorated effective lateral confining pressure distributed over the surface of the concrete core. Since, in general, a lack of experimental research and analytical studies on the confinement behaviour of corroded transverse ties under pitting corrosion exists in the literature (e.g.,[69]), a uniform corrosion model for area loss and reduction in confinement pressure is adopted (noting that most of the stress–strain models for confined concrete assume the lateral confining pressure from the ties to be uniformly distributed across the surface of the concrete core). This is considered a valid assumption based on a lifetime comparative assessment assuming both uniform and pitting area loss on columns' transversal ties performed by Shekhar et al.,[22] revealing negligible differences between the attained fragility estimates.

$$f'_{co} (\psi) = f'_c \left(2.254 \sqrt{1 + \frac{7.94 f_l (\psi)}{f'_c}} - 2 \frac{f_l (\psi)}{f'_c} - 1.254 \right) \tag{6}$$

It has been confirmed that non-uniform pit formations due to corrosion lead to potential reductions in the yield strength and ultimate strength of steel rebar (e.g.,[70,71]). The deteriorated yield strength and the deteriorated ultimate strength (denoted as $f_y(\psi)$ and $f_u(\psi)$, correspondingly) can be computed as in Equations (7) and (8), respectively. In these equations, $f_y(0)$ is the pristine yield strength, while $f_u(0)$ is the pristine ultimate strength. For uniform corrosion, the reductions in the strength values tend to be insignificant; thus, the reductions described are exclusively used for the pitting corrosion model (i.e., not applied for the transversal column ties). The described functional models are reliable up to $\psi = 25\%$, without extrapolation.

$$f_y (\psi) = (1 - 0.005\psi) \, f_y (0) \tag{7}$$

$$f_u (\psi) = (1 - 0.005\psi) \, f_u (0) \tag{8}$$

Based on a literature survey conducted by the authors, there is no clear agreement on the ultimate steel strain deterioration behaviour given corrosion deteriorating effects (e.g.,[72]). Therefore, based on relevant experimental results (e.g.,[73]), this study adopts a model in which the ultimate steel strain is nonlinearly correlated with the percentage of steel rebar area loss. The ultimate steel strain is estimated as shown in Equation (9) as in Biondini and Vergani.[74] $\varepsilon_u(\psi)$ and $\varepsilon_u(0)$ represent the deteriorated ultimate steel strain and the pristine ultimate steel strain, respectively.

$$\varepsilon_u (\psi) = \begin{cases} \varepsilon_u (0) & 0 \leq \psi < 1.6 \\ 0.1521 \left(\frac{\psi}{100} \right)^{-0.4583} \varepsilon_u (0) & 1.6 \leq \psi \leq 100 \end{cases} \tag{9}$$

To account for the impact of corrosion on the rebar steel buckling, Equation (10)[75] is used to modify their compression response (i.e., the post-buckling behaviour of the rebar steel). In this equation, $f_{yc}(\psi)$ is the deteriorated compressive yield steel strength, and L is the free length between the transversal column ties; $f_y(0)$ is the pristine yield strength (as introduced before). The length L is assumed to be invariant across the different corrosion deterioration levels (because a uniform corrosion model is assumed for the transversal column ties). In this study, the slenderness ratio for pristine steel

rebars equals 1.6.

$$f_{yc}(\psi) = \begin{cases} (1 - 0.0050\psi) f_y(0) & \frac{L}{d(\psi)} \le 6 \\ (1 - 0.0065\psi) f_y(0) & 6 < \frac{L}{d(\psi)} < 10 \\ (1 - 0.0125\psi) f_y(0) & \frac{L}{d(\psi)} \ge 10 \end{cases} \tag{10}$$

Regarding low-cycle fatigue, it has been demonstrated that the Coffin–Manson material constant $\alpha(\psi)$ is the only parameter affected by corrosion (e.g.,[75]); thus, other parameters remain unaltered. Equation (11) is utilised to calculate the $\alpha(\psi)$ parameter; $\alpha(0)$ corresponds to the material constant in pristine condition. It is worth observing that the bond strength deterioration is not considered in this study, since several other studies highlight that this feature has negligible contribution to the structural failure of corroding columns with transversal ties under cyclic loading (e.g.,[76]).

$$\alpha(\psi) = (1 - 0.004\psi) \, \alpha(0) \tag{11}$$

2.4 | Fragility and vulnerability

Due to the unsymmetric dynamic properties of the bridge structure in the two horizontal directions, the response significantly varies with the incidence of the ground-motion direction. Hence, for each considered ground-motion sequence, sequential cloud-based NLTHAs are conducted by rotating the two orthogonal components of the ground motions through 180° at 30° intervals. From the obtained bridge structural response in each rotating direction, the median of maximum column curvature (denoted as $Rot50\phi$) and the median of maximum shear-key displacement (denoted as $Rot50\Delta$) are obtained for the GM1, while the associated median of dissipated hysteretic energy (denoted as $Rot50E_H$) is obtained for both ground motions in the sequence (i.e., the portion of dissipated hysteretic energy achieved during the GM1 and GM2, separately). Note that in this EDP syntax, Rot indicates the rotation of the ground-motion components, and 50 indicates the percentile value used for the measure. The above-described analysis is repeated for the bridge structure at each corrosion deterioration level (i.e., ψ), capturing the structural response based on the dynamic structural behaviour exhibited given ground-motion sequences and corrosion deteriorating effects. In Figure 6A, $Rot50\phi$ versus $Rot50E_H$ relationships as a function of ψ are shown for an example column. It can be noticed that as the corrosion deterioration level increases, the structural capacity of the component decreases, from the fact that the illustrated relationships become asymptotically flat with ψ (i.e., lower hysteretic energy dissipation capacity as ψ increases). More details to derive state-dependent fragility and vulnerability relationships considering damage accumulation due to the seismic sequences and chloride-induced corrosion are presented in subsequent subsections.

2.4.1 | Damage-state definition

The DSs for columns are based on structure-specific DS descriptions for slight (DS1), moderate (DS2), extensive (DS3), and complete damage (DS4); DS0 indicates no damage. The column curvature (ϕ) is used to define the previous DSs. Specifically, the DS1 threshold is associated with the yielding strain of column rebars. At this level, concrete is assumed to be at the onset of visible cracking, and the curvature ductility demand is near 1. The DS2 threshold is associated with reaching ultimate strain in the extreme fibres of concrete cover. At this level (i.e., spalling strain), potential plastic hinges form due to slippage of the lap-splices (e.g.,[77,78]). The DS4 threshold is associated with the attainment of the ultimate strain of the extreme fibres of the concrete core (i.e., compression strain at which transverse column ties start to fracture; e.g.,[79, 80]) or the most stressed longitudinal steel rebar. Based on existing literature on corroding and pristine RC bridge columns (e.g.,[81]), the DS3 threshold is expected to be between DS2 and DS4 thresholds. Therefore, this study uses the geometric mean of the two (i.e., DS2 and DS4) as the DS3 threshold.[82] All the previous DS thresholds are calibrated using pushover analysis. Figure 5A shows the structure-specific column DSs mapping for the selected corrosion deterioration levels (M is the bending moment in a column associated with ϕ). The DSs for the shear keys are identified according to the mechanical model proposed by Kottari[53] and Omrani et al.,[49] for the same damage level descriptors defined already for columns. The shear-key displacement (Δ) is used to define the previous DSs. Given that the transversal behaviour of the abutments is
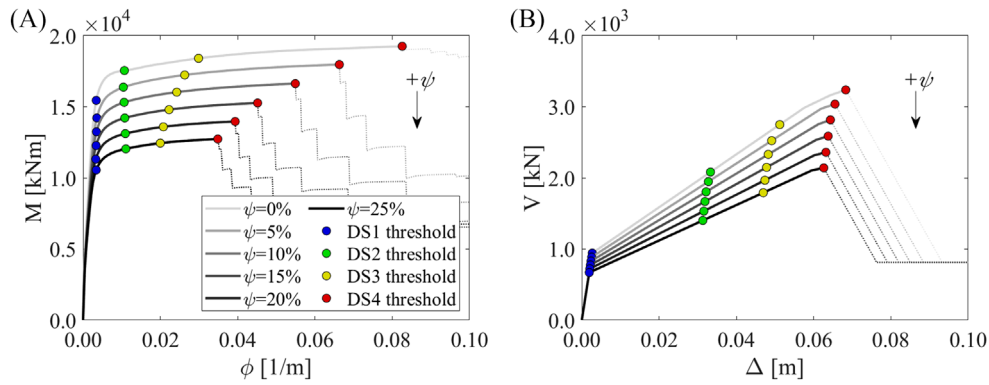
FIGURE 5 Bridge component DS threshold mapping: (A) Column DS thresholds; (B) shear-key DS thresholds. The corrosion deterioration level increased from the upper to the lower capacity curve with increasing colour intensity (i.e., grey to black)

TABLE 1 Coefficients of the functional prediction model for DS thresholds as a function of ψ

DS threshold	DS1					DS2				
	Mean	β_1	β_2	$\sigma_{1,DS1}$	R^2	β_1	β_2		$\sigma_{1,DS2}$	R^2
Column	3.26e-3	N/A	N/A	N/A	N/A	1.03e-2	3.16e-5		9.20e-5	0.93
Shear key	N/A	2.70e-3	−3.14e-5	5.46e-6	1.00	3.32e-2	−7.87e-4		1.56e-4	0.96
DS threshold	DS3					DS4				
	β_1	β_2	β_3	$\sigma_{1,DS3}$	R^2	β_1	β_2	β_3	$\sigma_{1,DS4}$	R^2
Column	2.97e-2	−6.79e-4	1.16e-5	2.49e-4	1.00	8.22e-2	−3.33e-3	5.80e-5	6.76e-4	1.00
Shear key	5.10e-2	−3.34e-4	7.21e-6	3.61e-4	0.97	6.80e-2	−4.46e-4	9.61e-6	4.81e-4	0.97

modelled as a combination of the abutment piles, the elastomeric bearing pads and the shear keys in this study, the DS1, DS2, DS3 and DS4 thresholds are associated with the yielding displacement, 50% of the ultimate displacement, 75% of the ultimate displacement and the ultimate displacement of the transversal system of springs, respectively (e.g.,[83]). The previous DS thresholds are calibrated using pushover analysis as well. It is worth mentioning that the shear keys are a sacrificial secondary component, and their failure does not influence the higher DS of the bridge structure (i.e., system). Figure 5B shows the structure-specific shear-key DSs mapping for the selected corrosion deterioration levels (V represent the shear force in a shear key associated with Δ).

To estimate the DSs thresholds as a function of ψ, functional prediction models are proposed with the form described in Equation (12). The associated coefficients (i.e., β_1, β_2, and β_3) are presented in Table 1 (R^2 is the coefficient of determination), calibrated through ordinary least-squares polynomial regression on the DS threshold values as appropriate (ε_1 is a normal random variable related with the error of the residuals with variance σ_1^2). An apparent linear trend can describe the deteriorating DS thresholds for DS1 and DS2 (for column DS1, the threshold can be simply estimated as the data mean because its associated values are near-constant but linear; i.e., $\beta_2 = 0$). In contrast, a near quadratic trend is noted for DS3 and DS4. The estimated regression coefficients are all significant, i.e., the fitted models have coefficients that differ significantly from zero. It is worth noting that the DS thresholds estimation is critical when assessing the seismic structural performance under deteriorating effects since the bridge response strongly varies with ψ (especially for columns), and the utilisation of constant DS thresholds become infeasible for fragility and vulnerability analysis in such case.

The bridge structure is considered to follow the series system assumption (e.g.,[82,84]); therefore, the system-level DSs are based on the occurrence of damage in relevant structural components (e.g.,[85]). In this study, each component is classified into primary and secondary ones based upon their importance in the bridge load-carrying capacity and overall bridge stability. Only the primary components, such as the columns or the deck that has reached its unseating DS threshold, are assumed to contribute to the extensive and complete DS of the bridge structure (i.e., DS3 and DS4). Since the loss of primary components directly affects the bridge load-carrying capacity and overall bridge stability, the primary components' specified DSs thresholds (i.e., DS3 and DS4) directly correspond to the bridge structure's DS thresholds. The secondary components (e.g., shear keys) - whose complete failure will not have a similar consequence as the primary ones - are assumed to contribute only to the prior system DSs (i.e., DS1 and DS2) (e.g.,[84]). In fact, the shear keys represent sacrificial

TABLE 2 Component-level DSs defining the system-level DSs

DSs description	Component-level DSs		System-level DSs
	Primary components	Secondary components	
Slight	DS1	DS3	DS1
Moderate	DS2	DS4	DS2
Extensive	DS3	N/A	DS3
Complete	DS4	N/A	DS4

components intended to fail before the abutments suffer extensive damage (commonly, secondary but not sacrificial components are assumed to contribute to DS1, DS2 and DS3). In Table 2, the component-level DSs defining the system-level DSs are presented for clarity. In this table, for example, system-level DS1 is determined by the columns' DS1 and the shear keys' DS3.

$$DSi_{threshold} = \begin{cases} \beta_1 + \beta_2\psi + \varepsilon_1 \sim N\left(0, \sigma_1^2\right) & i = 1, 2 \\ \beta_1 + \beta_2\psi + \beta_3\psi^2 + \varepsilon_1 \sim N\left(0, \sigma_1^2\right) & i = 3, 4 \end{cases} \tag{12}$$

2.4.2 | Probabilistic seismic demand model

The proposed vector-valued PSDMs (i.e., PSDM that is conditioned on a vector of parameters rather than a single parameter) are derived by fitting the response surface $E_{H,GM1GM2}(EDP_{GM1}, IM_{GM2})$, as proposed in Gentile and Galasso.[86] $E_{H,GM1GM2}$ is the total dissipated hysteretic energy in the sequence (i.e., in GM1 and GM2; i.e., the summation of their respective $Rot50E_H$ portions obtained during the sequence); EDP_{GM1} is the associated deformation-based EDP obtained during GM1 (representing $Rot50\phi$ or $Rot50\Delta$ depending on the component of analysis); and IM_{GM2} is the associated IM of the GM2 (defined earlier as $avgSA$). The $E_{H,GM1GM2}$ is adopted as the main EDP as it is a cumulative measure that monotonically increases with the length of the applied seismic excitation. Thus, unlike deformation-based parameters (e.g., $Rot50\phi$ or $Rot50\Delta$), this allows the development of statistical models consistent with the physics of damage accumulation characterising a bridge structure subjected to ground-motion sequences. The latter also avoids inconsistencies in the resulting statistical models due to inappropriate consideration of damage accumulation. The major drawback of using cumulative-based EDPs, as proposed in this study, is related to the DS thresholds definition. In fact, it is considered challenging to estimate component or global structural damage in terms of cumulative EDPs to define reliable DS thresholds that are more easily (and broadly) defined based on curvature/displacement. However, a stable, pseudo-parabolic relationship is usually observed between a maximum deformation parameter and dissipated hysteretic energy, as demonstrated by Gentile and Galasso through theoretical considerations and simulation results.[86] Hence, the maximum deformation–hysteretic energy relationship (i.e., $Rot50\phi$ vs. $Rot50E_H$ or $Rot50\Delta$ vs. $Rot50E_H$) is used to convert deformation-based DS thresholds into energy-based ones, permitting to retain the reliability of the adopted deformation-based DS thresholds.

The fundamental requirement for any PSDM is consistency with the physics of the problem under investigation; therefore, consistency with the relevant mechanics is achieved if: (a) $E_{H,GM1GM2}$ during the sequence is monotonic regarding EDP_{GM1} and IM_{GM2}[86]; and (b) for any given value of IM_{GM2}, $E_{H,GM2}$ (i.e., the $Rot50E_H$ during GM2; thus, $E_{H,GM1}$ is the $Rot50E_H$ during GM1) must be monotonically decreasing with respect to EDP_{GM1}.[86] Accordingly, a seven-parameter (i.e., a_0, b_0, c_0, d_0, e_0, f_0 and m_0) functional form for the vector-valued PSDMs is developed using Equation (13) (ε_2 is a log-normal random variable associated with the error of the residuals with variance σ_2^2). Thereby, for each critical structural component (i.e., columns and shear keys) in pristine condition (i.e., $\psi = 0\%$), a PSDM is developed individually based on the selected EDPs and IM. The steps to fit the proposed PSDMs are summarised as follows:

1. Using the data corresponding to GM1 only (i.e., EDP_{GM1}, $E_{H,GM1}$), the $E_{H,GM1} = \exp(a_0 EDP_{GM1}^{b_0} + c_0 EDP_{GM1}^{d_0})$ relationship is fitted. The parameters a_0, b_0, c_0 and d_0 are estimated through least-squares nonlinear regression in log–log space (Figure 6A). Such a model allows capturing the nonlinearities in the EDP_{GM1} versus $E_{H,GM1}$ relationship.
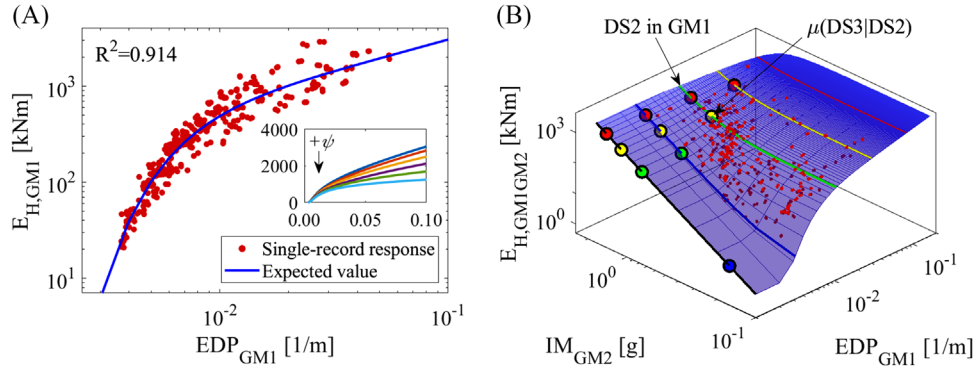
FIGURE 6 (A) $E_{H,GM1}$ relationship fit; (B) $E_{H,GM1GM2}$ relationship fit; for the bridge's column example case in pristine condition ($\psi = 0\%$). The black, blue, green, yellow, and red lines in (B) represent PSDMs conditioned on a deformation-based DS threshold for DS0, DS1, DS2, DS3 and DS4, respectively

TABLE 3 Coefficients of the functional prediction model for the parameterised vector-valued PSDM as a function of ψ for the bridge's column example case in pristine condition ($\psi = 0\%$)

Parameter	a_0	b_0	c_0	d_0	e_0	f_0	m_0	R^2
$\sigma_{2,ln(E_H)}= 0.59$	9.668	8.039e-2	−1.261e-4	−1.794	1.073e3	2.561	4.991	> 0.757
Parameter	a_1	b_1	c_1	d_1	e_1	f_1	m_1	R^2
$\sigma_{3,ln(E_H)}= 0.37$	−1.011e-1	−2.854e-3	−5.556e-6	1.814e-3	−4.248	−6.376e-3	2.866e-1	0.900

2. Using the data corresponding to GM1 only (i.e., IM_{GM1}, $E_{H,GM1}$), the $E_{H,GM1} = e_0\,IM_{GM1}^{f_0}$ relationship is fitted. The parameters e_0 and f_0 are estimated through ordinary least-squares linear regression in log–log space. This model follows the traditional power-law relationship, typically employed in cloud-based procedures.

3. Using the GM1 and GM2 data (i.e., EDP_{GM1}, IM_{GM2}, $E_{H,GM2}$), the parameter m_0 is estimated through least-squares nonlinear regression to the model $E_{H,GM2} = e_0\,(1 - m_0 EDP_{GM1})IM_{GM2}^{f_0}$. Herein, the parameters e_0 and f_0 are estimated as described in the previous point and used as constants. This is possible considering that a GM1 can be interpreted as a GM2 that follows a GM1 producing a zero EDP_{GM1} value (i.e., a GM2 that follows no GM1 is a GM1 itself).

$$E_{H,GM1GM2} = \exp\left(a_0 EDP_{GM1}^{b_0} + c_0 EDP_{GM1}^{d_0}\right) + e_0\,(1 - m_0 EDP_{GM1})IM_{GM2}^{f_0} + \varepsilon_2 \sim LN\left(0, \sigma_2^2\right) \tag{13}$$

To introduce the deteriorating effects in the developed models, the vector-valued PSDMs are further refined as shown in Equation (14) (employing the coefficients computed in Equation (13) in pristine condition as constants and the data associated with all the other corrosion deterioration levels), through least-squares nonlinear regression (ε_3 is a log-normal random variable associated with the error of the residuals with variance σ_3^2). A fitted median parameterised (i.e., dependent on the corrosion deterioration level) vector-valued PSDM (Figure 6B) and its coefficients and logarithmic standard deviation (computed as the root mean squared error of the residuals, RMSE) is illustrated for a bridge's column example case in pristine condition; this described process is repeated for every deteriorating component. The associated coefficients (i.e., a_0, b_0, c_0, d_0, e_0, f_0, m_0, a_1, b_1, c_1, d_1, e_1, f_1, and m_1) and the logarithmic standard deviation (in terms of RMSE) are presented in Table 3. It is worth mentioning that the dispersion of the structural response increase with the corrosion deterioration level; however, given the vector-valued PSDM modelling approach (i.e., cloud-based analysis through linear/nonlinear regression using the least-squares approach), a single value of dispersion will be obtained for all the state-dependent fragility relationships of a structural component regardless of the ψ. Although, this is not deemed an issue since the relative variation between the dispersion in pristine conditions and at the highest corrosion deterioration level (i.e.,

$\psi = 25\%$) is less than 5%.

$$E_{H,GM1GM2} = \exp\left[(a_0 + a_1\psi) EDP_{GM1}^{b_0+b_1\psi} + (c_0 + c_1\psi) EDP_{GM1}^{d_0+d_1\psi}\right]$$

$$+ (e_0 + e_1\psi)[1 - (m_0 + m_1\psi) EDP_{GM1}] IM_{GM2}^{f_0+f_1\psi} + \varepsilon_3 \sim LN\left(0, \sigma_3^2\right) \tag{14}$$

2.4.3 | State-dependent fragility

The proposed median parameterised vector-valued PSDMs are used to derive state-dependent fragility relationships for each deteriorating structural component. As shown in Figure 6A, after selecting the deformation-based DS thresholds ($\overline{EDP_{DS}}$) for each DS (Figure 5A,B), a PSDM provides the corresponding dissipated hysteretic energy-based DS thresholds ($\overline{E_{H,DS}}$) (note that these DS thresholds are also dependent on ψ, but this is not indicated for brevity). Equation (15) allows deriving fragility relationships for different combinations of the DS in both the GM1 and GM2 given a corrosion deterioration level, denoted as $F(DS_{GM2}|DS_{GM1})$; where DS_{GM1} is always lower than DS_{GM2}. Practically, $F(DS_{GM2}|DS0)$ are the GM1 fragility relationships of a structure pre-damaged exclusively by corrosion (if present), while $F(DS_{GM2}|DS_{GM1})$ represents the GM2 fragility relationship conditioned on a given DS in the GM1 (hence, provide the sequential fragility relationships) and corrosion. In Equation (15), $\mu(DS_{GM2}|DS_{GM1})$ is the fragility median value, while $\sigma(DS_{GM2}|DS_{GM1})$ is the logarithmic standard deviation of the PSDM (in terms of RMSE as estimated above). Using the deformation-based DS thresholds for GM1 and the computed energy-based DS threshold for GM2, by inverting Equation (14), the median of a given fragility relationship is computed using Equation (16). The associated dispersion related to the record-to-record variability is computed using Equation (17). This dispersion is further augmented (by the square root of the sum of the squares) to propagate the uncertainty related to the strength of the materials (i.e., β_c) and the modelling of the structural components (i.e., β_m) with values of 0.25 and 0.39, respectively (e.g.,[26,87]). It is worth mentioning that the dynamic analyses leading to collapse are disregarded for simplicity, but the information carried out by such data can be considered when deriving the fragility relationships (e.g.,[88]).

$$F(DS_{GM2}|DS_{GM1}) = P\left(E_{H,GM1GM2} \geq \overline{E_{H,DS}}|IM, DS_{GM1}, \psi\right) = 1 - \Phi\left[\frac{ln\left(\overline{E_{H,DS}}\right) - \mu(DS_{GM2}|DS_{GM1})}{\sigma(DS_{GM2}|DS_{GM1})}\right] \tag{15}$$

$$\mu(DS_{GM2}|DS_{GM1}) = \left\{\frac{\overline{E_{H,DS}} - \exp\left[(a_0 + a_1\psi)\overline{EDP_{DS}}^{b_0+b_1\psi} + (c_0 + c_1\psi)\overline{EDP_{DS}}^{d_0+d_1\psi}\right]}{(e_0 + e_1\psi)\left[1 - (m_0 + m_1\psi)\overline{EDP_{DS}}\right]}\right\}^{1/(f_0+f_1\psi)} \tag{16}$$

$$\beta(DS_{GM2}|DS_{GM1}) = \frac{\sigma(DS_{GM2}|DS_{GM1})}{f_0 + f_1\psi} \tag{17}$$

The bridge structure is regarded as a series system to conduct the fragility analysis at the system level. Each component is classified into primary (i.e., columns) and secondary (i.e., shear keys) ones based on their importance in the bridge load-carrying capacity and overall bridge stability, as mentioned before. Therefore, the bridge structure fragility relationships for DS_{GM2} conditioned on DS_{GM1} (for the ith DS_{GM2} and the kth DS_{GM1}), can be jointly evaluated using Equation (18) (i.e., a multivariate normal distribution as joint PSDM), where p indicates the number of primary components and s indicates the number of secondary components. The equation is evaluated using the developed PSDMs for the bridge's components dependent on the deformation-based DS threshold (coloured lines in Figures 6B and 7A). This is done by interchanging EDP_{GM1} with 0 for single-shock damaging condition and for $\overline{EDP_{DS}}$ of the desire DS threshold for multiple-shock damaged condition in Equation (14). Such equation provided two-dimensional ($avgSA$ vs. $E_{H,GM1GM2}$, for a specific corrosion deterioration level) PSDMs conditioned on a previous DS, an IM and a ψ (Figure 7A). It is worth noting that k
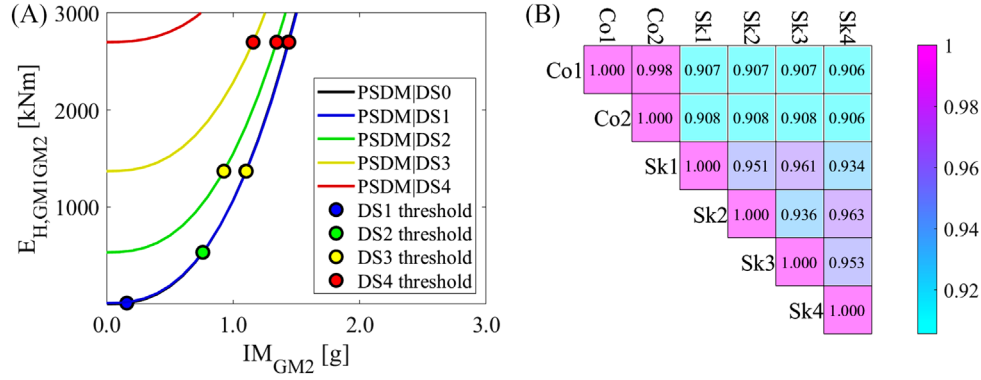
FIGURE 7 (A) Bridge's column example case conditioned PSDMs and DS thresholds for simulating response demands in pristine condition ($\psi = 0\%$); (B) correlation matrix between the bridge component's response (Co and Sk stand for column and shear key, correspondingly; the case-study ordinary bridge has two columns and four shear keys).
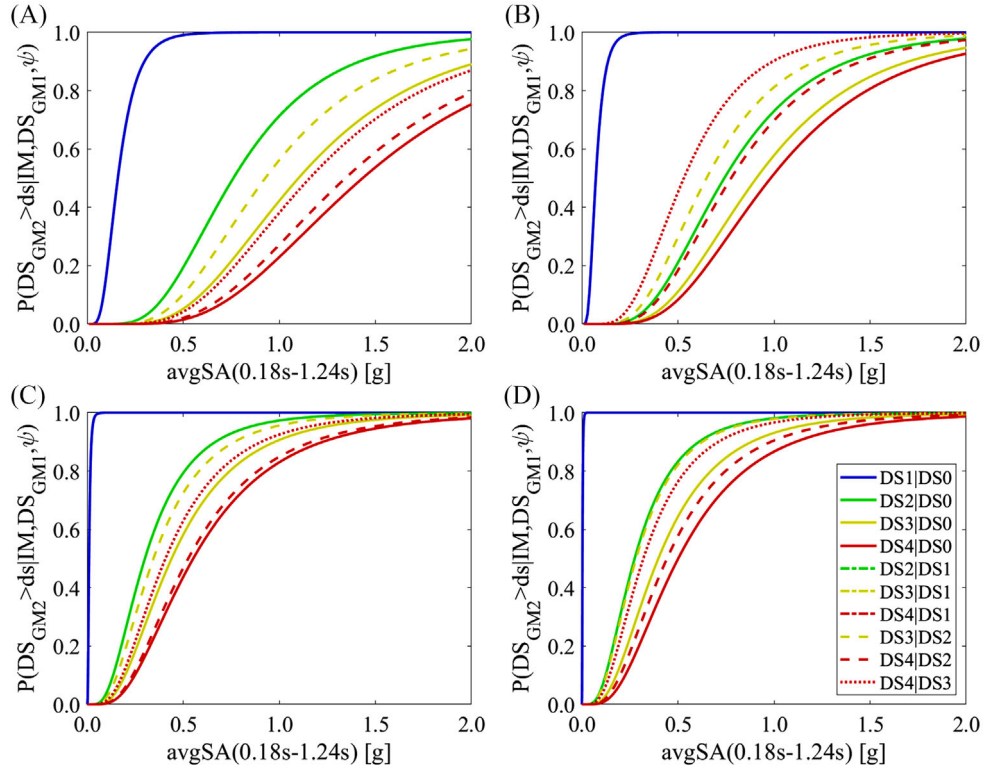
is always lower than i.

$$F\left(DS_{GM2}|DS_{GM1}\right) = \begin{cases} \bigcup_{b=1}^{p} F_b\left(DS_{GM2,i}|DS_{GM1,k}\right) & i > 2 \\ \bigcup_{a=1}^{s} F_a(DS_{GM2,i+2|}|DS_{GM1,k}) + \bigcup_{b=1}^{p} F_b\left(DS_{GM2,i}|DS_{GM1,k}\right) & i \leq 2 \end{cases} \tag{18}$$

Specifically, to derive the system-level state-dependent fragility relationships, a large sample of response estimates ($E^{sim}_{H,GM1GM2_t}$) from the component-specific PSDMs at different $avgSA$ intensity levels (IM_j) are obtained through a component-based Monte-Carlo approach. To do so, at a specific IM_j, an uncorrelated standard normal random vector (with u^{sim}_t elements) is sampled with p entries for DS3 and DS4, or $s + p$ entries for other DSs (with t entries in total). Using the previous uncorrelated vector, a correlated standard normal random vector (with v^{sim}_t elements) is attained using the Cholesky decomposition of the component's response correlation matrix (computed employing Pearson correlation coefficients in log–log space, Figure 7B). The structural response estimates are calculated as seen in Equation (19) for each component using the correlated vector. $\mu(DS_{GM2}|DS_{GM1})_t$ is the median value and $\sigma(DS_{GM2}|DS_{GM1})_t$ is the logarithmic standard deviation for each component conditioned PSDM. The above process is repeated 10,000 times per each IM_j, this number is calibrated based on a sensitivity analysis developed by the authors to obtain stable results. Note, before starting the above-described process, the conditioned PSDMs (e.g., Figure 7A) need to be shifted to the origin (i.e., the first coordinate of the models coincides with the origin); the DSs thresholds are shifted proportionally.

$$E^{sim}_{H,GM1GM2_t} = \exp\left\{ ln\left[\mu(DS_{GM2}|DS_{GM1})_t\right] + \sigma(DS_{GM2}|DS_{GM1})_t v^{sim}_t \right\} \tag{19}$$

The structural response estimates for a given IM_j are then compared against the corresponding component-specific DS thresholds; a binary vector of ones on whether the response exceeds the respective DS threshold or zeros otherwise is assembled. A matrix of the binary elements wherein each matrix column corresponds to the binary vectors for each component is assembled afterwards. A system-level binary vector is then built, where the ith element is equal to one if any one of the elements in the ith row of the matrix equals one and is equal to zero otherwise (the system-level binary vector is obtained for each IM_j). The results are used to obtain the fragility relationship parameters (i.e., median and dispersion) by maximising the logarithm of the likelihood function[89] shown in Equation (20). In this equation, im is the total number of IM_j; y_j and z_j are the number of exceedances (i.e., number of ones) and the total observations (i.e., 10,000), respectively; μ and β are the fragility median value and dispersion guesses, respectively (the method of moments is employed to get the values for the initial guess of these parameters); and $\hat{\mu}$ and $\hat{\beta}$ are the fragility median value and dispersion attained from the maximisation process.

$$\left(\hat{\mu}, \hat{\beta}\right) = \arg\max_{\mu,\beta} \sum_{j=1}^{im} \left\{ ln\binom{y_j}{z_j} + z_j ln\left(\Phi\left[\frac{ln\left(IM_j/\mu\right)}{\beta} \right] \right) + (y_j - z_j) ln\left(1 - \Phi\left[\frac{ln\left(IM_j/\mu\right)}{\beta} \right] \right) \right\} \tag{20}$$

FIGURE 8 (A) State-dependent fragility relationships of the bridge columns for the pristine condition ($\psi = 0\%$); and (B) for the deteriorated condition ($\psi = 25\%$); (C) state-dependent fragility relationships of the bridge shear keys for the pristine condition ($\psi = 0\%$); and (D) for the deteriorated condition ($\psi = 25\%$)

2.4.4 | State-dependent vulnerability

Damage-to-loss ratios (DLRs) are usually estimated empirically through post-earthquake reconnaissance or employing expert judgment. These ratios are site- and bridge-specific and must be carefully selected while developing vulnerability relationships. For this study, the DLRs suggested by Padgett et al.[90] implemented in regional seismic risk analysis of bridge networks are considered. Hence, the damage-to-loss ratios used in this study correspond to: (a) 0.00 for DS0; (b) 0.03 for DS1; (c) 0.15 for DS2; 0.40 for DS3; and 1.00 for DS4 (for the system-level only). Vulnerability relationships are expressed in terms of mean loss ratio (LR) or the repair-to-replacement cost ratio of a bridge conditional on $avgSA$. Such relationships are derived through Equation (21) using the total probability theorem. In such an equation, DLR_i is the DLR for the ith DS_{GM2}. It should also be noted that the LR values at $avgSA = 0$ g intensity level are equivalent to the LR values of the DSs caused by GM1 (i.e., the expected LR associated with the kth DS_{GM1} reached when GM1 has already occurred set as constant) or zero for no damage caused by GM1 (i.e., utilising fragility relationships conditioning on DS0). It is worth noting that k is always lower than i.

$$LR(IM, DS_{GM1}, \psi) = \sum_{i=1}^{4} DLR_i \left[F\left(DS_{GM2,i} | DS_{GM1,k}\right) - F\left(DS_{GM2,i+1} | DS_{GM1,k}\right) \right] \quad (21)$$

3 | RESULTS AND DISCUSSION

3.1 | State-dependent fragility relationships for bridge components

The state-dependent fragility relationships for the bridge critical components (i.e., bridge columns and shear keys) are derived for the pristine condition ($\psi = 0\%$) (Figure 8A,C) and deteriorated condition ($\psi = 25\%$) (Figure 8B,D) to show the impact of chloride-induced corrosion deterioration at the component level (utilising the parameterised vector-valued

TABLE 4 State-dependent fragility relationship parameters for structural components with $\psi = 0\%$ and $\psi = 25\%$

Component/ Parameter [g]	Column ($\psi = 0\%$)	Column ($\psi = 25\%$)	Shear key ($\psi = 0\%$)	Shear key ($\psi = 25\%$)	Rel. var. (%) (column)	Rel. var. (%) (shear key)
$\mu(DS1|DS0)$	0.18	0.08	0.01	<0.01	115.88	218.40
$\mu(DS2|DS0)$	0.75	0.74	0.30	0.27	0.43	9.47
$\mu(DS3|DS0)$	1.10	0.92	0.44	0.40	19.95	10.50
$\mu(DS4|DS0)$	1.41	0.99	0.55	0.50	42.96	10.12
$\mu(DS2|DS1)$	0.74	0.74	0.30	0.27	0.12	9.47
$\mu(DS3|DS1)$	1.10	0.92	0.44	0.40	19.95	10.50
$\mu(DS4|DS1)$	1.41	0.99	0.55	0.50	42.96	10.12
$\mu(DS3|DS2)$	0.94	0.65	0.34	0.28	43.11	22.30
$\mu(DS4|DS2)$	1.32	0.77	0.53	0.44	70.99	18.76
$\mu(DS4|DS3)$	1.13	0.51	0.41	0.32	120.36	27.40
β	0.49	0.49	0.62	0.62	N/A	N/A

The most deteriorated condition is utilised as a benchmark case to estimate the relative variation.

PSDMs). It is observed that the fragility relationships are consistently shifted to the left when ψ increase (Table 4), indicating a reduction of the fragility median values for a given corrosion deterioration level during a ground-motion sequence. The reduction in fragility median values is more apparent for the columns since the deteriorating effects on the column hysteretic response are better captured using the fibre-section modelling technique and due to its strong strength and curvature capacity deterioration. This is not the case for shear keys, where the hysteretic response is slightly affected compared to the columns, with a significant reduction in the shear strength, but not in the displacement capacity (by inspecting Figure 5, it could be noticed that the DS thresholds do not vary significantly with the deteriorating effects). It is observed that the dissipated hysteretic energy in the shear keys increases marginally as the $avgSA$ values increase; in contrast, the dissipated hysteretic energy in the columns significantly increases for the same $avgSA$ intensity level (given their higher hysteretic energy dissipation capacity). Therefore, it is inferred that shear keys reach their ultimate capacity for a relatively low $avgSA$ increment after the yielding displacement. The previous is consistent with the nature of those components since they are sacrificial elements to avoid extensive damage in the abutments, differing from the much stronger columns, which are components influencing the load-carrying capacity and overall bridge stability. It can also be noticed that the dispersion for the columns is lower than the one obtained for the shear keys, given the higher scatter of the shear keys' response values. This is because of the unsymmetric dynamic properties of the bridge structure, where the response significantly varies with the incidence of the ground-motion direction (shear keys exclusively function in the transversal direction of the bridge). From the perspective of ground-motion sequences, in the case of the columns, all the fragility median values are significantly reduced concerning the ones attained for the undamaged structure (i.e., conditioning on DS0), except for the ones conditioned on DS1, which remain unchanged (i.e., the fragility relationships conditioned on DS0 and DS1 overlap). The latter is because the dissipated hysteretic energy by a structural component before the yielding point (i.e., the point associated with the deformation-based DS threshold for DS1) is nearly zero. In other words, the energy-based DS threshold for DS1 will be near zero regardless of the peak-based one, particularly for structural components. For the shear key, the observed behaviour is consistent with that of the columns to a lesser degree. The DS4|DS3 fragility relationship is significantly more shifted to the left (the hysteretic energy dissipated after DS3 is lower for this case than other DSs) as expected. It is worth mentioning that the deteriorating behaviour of columns has a pronounced effect on the dissipated hysteretic energy versus rotation relationship, having an asymptotic behaviour; this occurs in the shear keys as well, although such behaviour would emerge for unphysically large values of displacement considering their significant lower deterioration. The previous is because the dissipated hysteretic energy depends on the input energy of a ground motion, which always increases as the intensity level increases. In general, it is observed that DS1 and DS2 remain unaffected by the effects of the sequences; therefore, damage accumulation is more substantial for the higher DSs, when the components are at the onset of their ultimate (i.e., peak) strength and are about or start to strain-soften (i.e., DS3 and DS4).

To study the impact of chloride-induced corrosion deterioration in more detail, the proposed parameterised vector-valued PSDM for an example column is utilised to derive state-dependent fragility relationships at various deterioration levels (i.e., $\psi = 0\%$, $\psi = 8\%$, $\psi = 16\%$ and $\psi = 25\%$) in median terms. The fragility relationships DS3 and DS4 for an
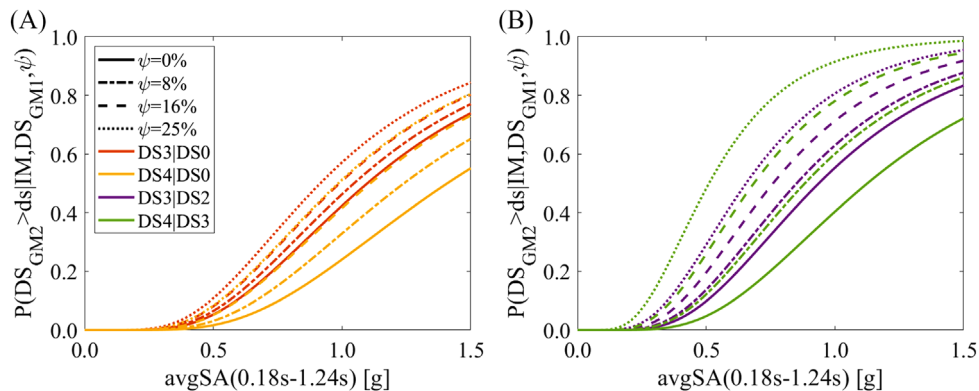
FIGURE 9　(A) DS4|DS0 and DS3|DS0; and (B) DS4|DS3 and DS3|DS2 fragility relationships for various corrosion deterioration levels (i.e., 0%, 8%, 16% and 25%) for the example bridge column

TABLE 5　State-dependent fragility relationship parameters for the example bridge column with $\psi = 0\%$, $\psi = 8\%$, $\psi = 16\%$ and $\psi = 25\%$

Component/ Parameter [g]	Column ($\psi = 0\%$)	Column ($\psi = 8\%$)	Column ($\psi = 16\%$)	Column ($\psi = 25\%$)	Rel. var. (%) ($\psi = 0\%-8\%$)	Rel. var (%) ($\psi = 0\%-25\%$)
$\mu(DS3|DS0)$	1.10	1.05	0.99	0.92	4.95	19.95
$\mu(DS4|DS0)$	1.41	1.24	1.11	0.99	13.56	42.96
$\mu(DS3|DS2)$	0.94	0.85	0.76	0.65	10.08	43.11
$\mu(DS4|DS3)$	1.13	0.88	0.69	0.51	27.49	120.36
β	0.49	0.49	0.49	0.49	N/A	N/A

The most deteriorated condition is utilised as a benchmark case to estimate the relative variation.

undamaged (Figure 9A) and damaged (Figure 9B) column are examined since these DSs are more impacted by deteriorating effects (given that corrosion-induced deterioration strongly reduces the column's curvature capacity at those DSs). Relative variations (with $\psi = 25\%$ case as benchmark) up to ~43% between the DS4|DS0, $\psi = 0\%$ and DS4|DS0, $\psi = 25\%$ (~120% between the DS4|DS3, $\psi = 0\%$ and DS4|DS3, $\psi = 25\%$) and up to ~20% between the DS3|DS0, $\psi = 0\%$ and DS3|DS0, $\psi = 25\%$ (~43% between the DS3|DS2, $\psi = 0\%$ and DS3|DS2, $\psi = 25\%$) in the fragility median values are observed from the analyses. It is evident that the variations for a given conditioned DS in a ground-motion sequence increase with ψ. Hence, the fragility median values decrease during a ground-motion sequence, but this reduction is aggravated with an increase in ψ. In general terms, the fragility median values reduce as ψ increases given a ground-motion sequence (Table 5), and the variations between the undamaged and the damaged (conditioned on a previous DS) respective values are higher in deteriorated components than for those in pristine conditions. This trend is more easily observed in Figure 10, where the fragility median values are plotted as a function of ψ. The larger reduction in the fragility median values (i.e., smaller bridge structure capacity) for higher conditioning DSs is due to the reserved dissipated hysteretic capacity after a GM1 is reduced as the DS increase due to component's strength and curvature/displacement capacity deterioration (i.e., the portion of dissipated hysteretic energy during GM2 is lower as the deformation-based EDP obtained during GM1 increase), especially for columns which possess higher dissipated hysteretic energy capacities governed by their flexural behaviour. The corrosion deteriorating effects strongly exacerbate the previous process. It is worth mentioning that the state-dependent fragility relationships derived conditioned on DS0 are equivalent to those obtained when performing an analysis under individual ground motions. Conceptually speaking, those relationships correspond to a GM2 that follows a GM1 producing a zero-response value.

3.2 | State-dependent fragility relationships for bridge structure

The proposed component-specific parameterised vector-valued PSDMs (e.g., Figure 7A) are jointly utilised (i.e., through a joint PSDM) to derive state-dependent fragility relationships using the described component-based Monte-Carlo approach for the bridge structure. A particular case for the bridge for a deteriorated ($\psi = 25\%$) condition is shown in
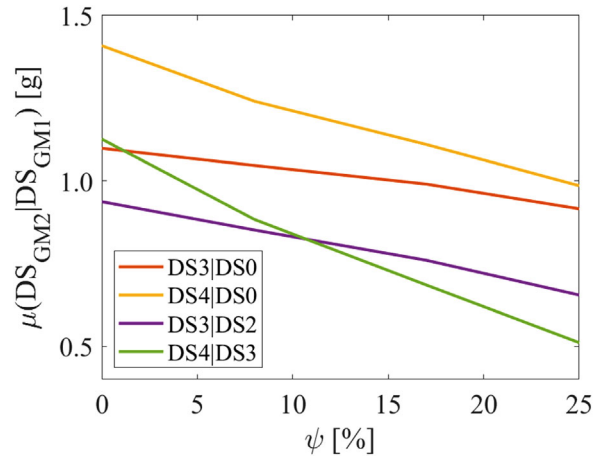
FIGURE 10 Trends in the state-dependent fragility median values as a function of ψ, for fragility relationships associated with the DSs: DS3|DS0, DS3|DS2, DS4|DS0 and DS4|DS3
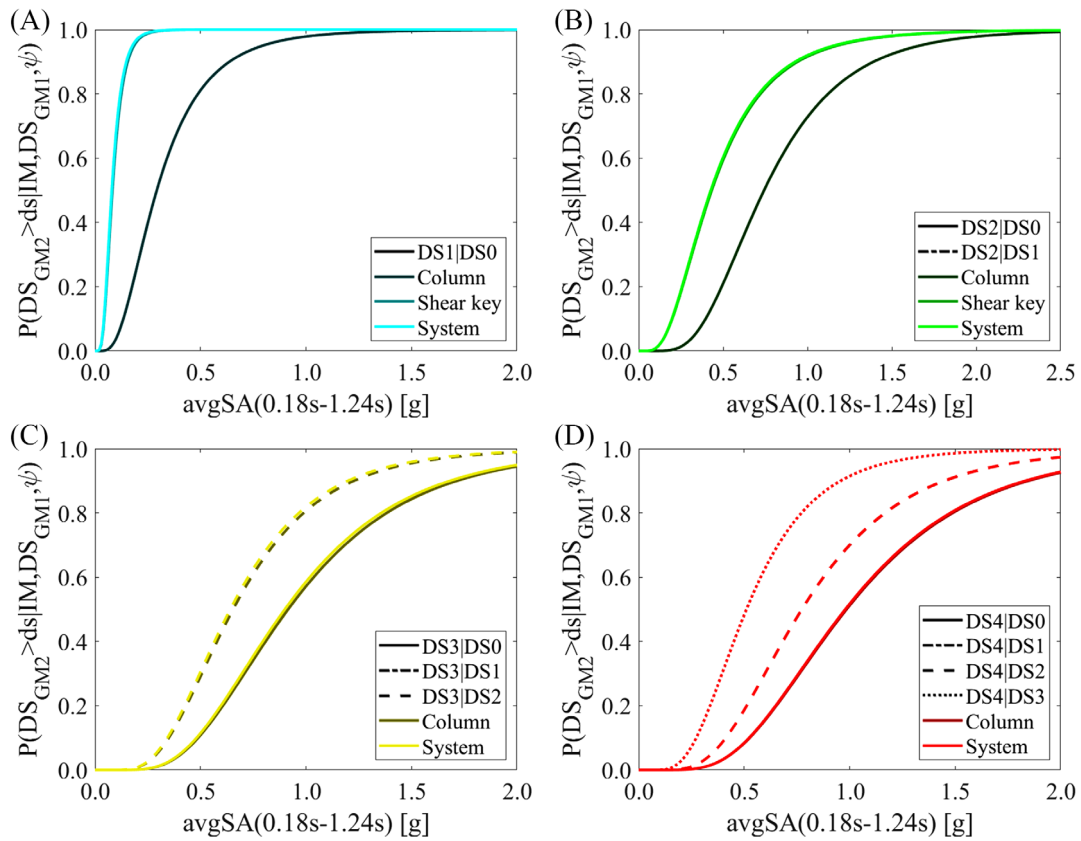
FIGURE 11 Bridge-structure state-dependent fragility relationships at a deteriorated ($\psi = 25\%$) condition for: (A) DS1; (B) DS2; (C) DS3; and (D) DS4; conditioned on a previous DSs as appropriate

Figure 11A–D; nevertheless, the results described here (related to the derivation of system-level state-dependent fragility relationships) are consistent regardless of the conditioning ψ. It can be seen that the system's fragility relationships are controlled by the columns (except for the one related to DS2, which is controlled by the shear keys). The trend mentioned before occurs because there are no crossing fragility relationships as it can occur depending on the structural characteristics. Therefore, when considering DS1 and DS2 (Figure 11A,B), the system-level fragility relationship corresponds to the most fragile component's fragility relationship. For DS3 and DS4 (Figure 11C,D), since columns are
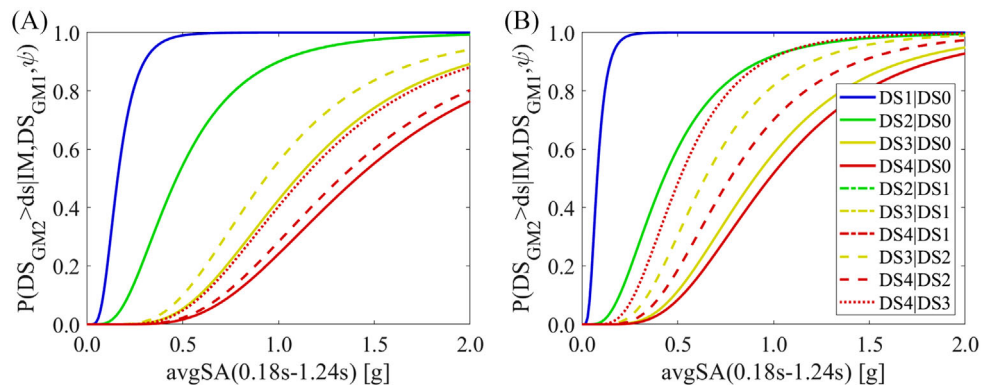
FIGURE 12 Bridge-structure state-dependent fragility relationships for: (A) pristine condition ($\psi = 0\%$); and (B) deteriorated ($\psi = 25\%$) condition; for all the DSs conditioned on a previous DS as appropriate

TABLE 6 State-dependent fragility relationship parameters for the system (i.e., bridge structure) with $\psi = 0\%$ and $\psi = 25\%$

Parameter [g]/ DSs	System μ ($\psi = 0\%$)	System β ($\psi = 0\%$)	System μ ($\psi = 25\%$)	System β ($\psi = 25\%$)	Rel. var. [%] (System μ)
$DS1|DS0$	0.16	0.49	0.08	0.49	102.49
$DS2|DS0$	0.47	0.60	0.43	0.60	9.35
$DS3|DS0$	1.10	0.49	0.90	0.49	21.66
$DS4|DS0$	1.41	0.49	0.98	0.49	43.91
$DS2|DS1$	0.47	0.60	0.43	0.60	9.35
$DS3|DS1$	1.10	0.49	0.90	0.49	21.66
$DS4|DS1$	1.41	0.49	0.98	0.49	43.91
$DS3|DS2$	0.93	0.49	0.64	0.49	45.35
$DS4|DS2$	1.32	0.49	0.77	0.49	71.00
$DS4|DS3$	1.13	0.49	0.51	0.49	120.49

The most deteriorated condition is utilised as a benchmark case to estimate the relative variation.

the analysed primary components (observing that there are no ground-motion sequences causing bridge unseating), it can be noticed that the component and system fragility relationships are very similar. The slight difference arises from the variation in columns' response (the axial load in the columns may vary the response because of geometric nonlinearities). However, as seen when estimating the correlation between the component's response (Figure 7B), the structural response in the columns is almost positively fully correlated (i.e., correlation coefficient almost equals one). For the bridge-structure fragility, the fragility median values also reduce as ψ increases given a ground-motion sequence. The differences given the undamaged and the damaged state are higher in deteriorated components than in the pristine condition, as mentioned above. Figure 12A,B shows the state-dependent fragility relationships for the bridge structure for the pristine ($\psi = 0\%$) and deteriorated ($\psi = 25\%$) conditions, respectively; obtained by combining the derived bridge-structure state-dependent fragility relationships presented in Figure 11A–D. Relative variations (with $\psi = 25\%$ case as a benchmark) in the fragility median value span between ~9% and up to ~120% for this particular case (Table 6).

3.3 | State-dependent vulnerability relationships for bridge structure

From the derived system's state-dependent fragility relationships, state-dependent vulnerability relationships are developed through bridge-specific damage-to-loss models and the total probability theorem. Figure 13A shows the vulnerability relationships for the pristine ($\psi = 0\%$) and deteriorated ($\psi = 25\%$) condition. As expected, the vulnerability relationship conditioned on DS1 does not differ significantly from the one conditioned on DS0 (except minimally for the lower tail portion of the curve near zero, where the relationship conditioned on DS1 start at the corresponding LR associated with
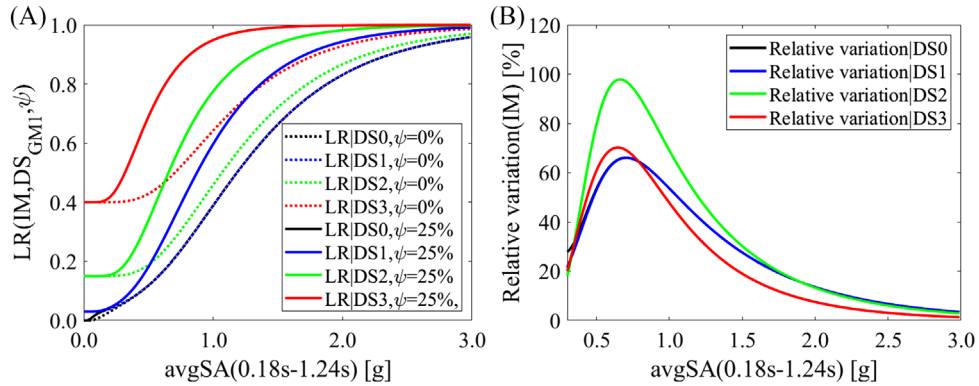
FIGURE 13 Bridge-structure state-dependent vulnerability relationships for: (A) pristine condition ($\psi = 0\%$); and deteriorated ($\psi = 25\%$) condition; (B) relative variation between the curves with $\psi = 0\%$ and $\psi = 25\%$ ($\psi = 0\%$ is used as a benchmark case)

this DS). For other conditioning DSs, the LR values increase in two ways. Firstly, the initial loss corresponds to the LR expected value for the respective conditioning DS. Secondly, the curves shift consistently to the left, indicating that the LR for the same $avgSA$ level increases when increasing ψ (this effect is propagated directly from the state-dependent fragility relationships). Figure 13B illustrates the relative variation between the vulnerability relationships for the pristine and deteriorated condition. The impact of corrosion deterioration is highly apparent, with a difference in LR at $avgSA = 0.65$ g (as an example) level of ~65% for LR|DS0, ~65% for LR|DS1, ~98% for LR|DS2, and ~70% for LR|DS3 (the relative variations depend directly on the intensity level). The results confirmed the intensified reduction of bridge seismic structural performance under a ground-motion sequence and subjected to corrosion deteriorating effects. It is worth mentioning that, as in state-dependent fragility relationships, the state-dependent vulnerability relationships derived conditioned on DS0 are equivalent to those attained when performing analyses under individual ground motions; since these are a direct propagation of the fragility analysis results.

4 | CONCLUSIONS

This study presents a novel framework for fragility and vulnerability analysis of deteriorating ordinary bridges under simulated ground-motion sequences. Parameterised vector-valued PSDMs are derived for bridge components using simulated ground-motion sequences attained from the CyberShake 15.12 ground-motion database. These models are directly used to derive state-dependent fragility relationships at the component level. The same models are then used to derive state-dependent fragility relationships at the system level, utilising a component-based Monte-Carlo approach. The results are finally combined with appropriate damage-to-loss models to derive state-dependent vulnerability relationships for the bridge structure. The total dissipated hysteretic energy in the seismic sequence is adopted as the main EDP because it is a cumulative-based measure that monotonically increases with the length of the applied seismic excitation. This parameter allows developing statistical models consistent with the physics of a bridge structure subjected to ground-motion sequences, unlike peak-based parameters. The finally derived state-dependent fragility and vulnerability relationships can be used, in general, for various regions, given that $avgSA$ reduces any bias due to non-site-specific, non-hazard-consistent ground-motion record selection.

The framework provides the means for assessing the seismic structural performance of ordinary bridges under individual ground motions or ground-motion sequences during their design lifetime. Additionally, given that a significant part of the worldwide bridge portfolio suffers from deteriorating effects due to corrosion, the framework can also help assessing the impact of corrosion-induced deterioration (specifically, chloride-induced corrosion) under any of the settings mentioned above. The outcomes from the developed framework (i.e., state-dependent fragility and vulnerability relationships) can be utilised for assessing an ordinary bridge seismic structural performance at a certain point in time or in a life-cycle type of analysis; for a single-bridge (with the above-pointed limitations) or a portfolio of bridges. The latter can be simply performed through a simulation process where firstly, the bridge structure's state of damage is sampled from fragility relationships given a first ground motion, and secondly (depending on whether retrofit actions occur or not), the loss ratio is estimated from vulnerability relationships given a second ground motion, accounting for the damage

accumulated due to corrosion or not. The average spectral accelerations (for the first and subsequent ground motions) can be obtained through event-based probabilistic seismic hazard analysis for the bridge lifetime using an appropriate rupture occurrence model according to the ground-motion sequences in the analysis. The ψ of interest can be obtained from the corrosion rate (i.e., the time-dependent steel rebar radius loss) depending on the environmental exposure scenario (e.g., marine atmospheric, marine sea-splash, deicing salt), from where it is easy to estimate how this corrosion rate varies in time (after the corrosion initiation time). Therefore, the developed state-dependent fragility and vulnerability relationships implicitly depend on time.

In general, it was observed that the effects of ground-motion sequences and corrosion-induced deterioration are more apparent in columns (components with high strength and displacement capacity) rather than abutment shear keys (components with low strength and displacement capacity). Hence, the importance of accounting for the interaction of these hazardous mechanisms given the low (to null) structural redundancy of some bridge structures (i.e., a significant decrease in columns' strength can signify the overall loss of bridge stability) is highlighted. Further investigation on the effects of corrosion on shear keys is suggested. It is also noted that the impact of the ground-motion sequences is exacerbated by corrosion deteriorating effects, in terms of reduced fragility median values comparing a pristine against a deteriorated structural component or the system, where these values reduce dramatically as the corrosion deterioration level increases. Furthermore, the bridge vulnerability (in terms of loss ratio) can increase in two main ways, as the corrosion deterioration level grows or the pre-damaged state grows. It is essential to notice that the corresponding loss ratio values are intensified when these hazards interact with respect to the case of individual hazard analyses (i.e., seismic- or environmentally induced).

The findings of this study provide evidence that sequential ground motions and corrosion-induced deterioration can play an important role in the structural response and damage/loss of ordinary bridges. Therefore, these multi-hazard threats must be considered, and strategies to account for those need to be implemented in current performance-based or seismic risk assessment practice, primarily when bridge structures that are susceptible to damage accumulation are investigated.

DATA AVAILABILITY STATEMENT
The data that support the findings of this study are available from the corresponding author upon reasonable request.

ORCID
Kenneth Otárola https://orcid.org/0000-0002-5425-4423
Jawad Fayaz https://orcid.org/0000-0003-4706-9761
Carmine Galasso https://orcid.org/0000-0001-5445-4911

REFERENCES
1. Caltrans. *Seismic Design Criteria. Version 2.0*. Sacramento, CA: California Department of Transportation; 2019.
2. Fayaz J, Xiang Y, Zareian F. Performance assessment of bridges under a sequence of seismic excitations. In: Papadrakakis M, Fragiadakis M, eds. 7th ECCOMAS Thematic Conference on Computational Methods in Structural Dynamics and Earthquake Engineering (COMPDYN). Vol 2. Eccomas Proceedia; 2019:2661-2676. doi:10.7712/120119.7101.19241
3. Ghosh J, Padgett JE, Sánchez-Silva M. Seismic damage accumulation in highway bridges in earthquake-prone regions. *Earthq Spectra*. 2015;31(1):115-135. doi:10.1193/120812EQS347M
4. Jayadipta G, E PJ. Aging considerations in the development of time-dependent seismic fragility curves. *J Struct Eng*. 2010;136(12):1497-1511. doi:10.1061/(ASCE)ST.1943-541X.0000260
5. Dizaj EA, Padgett JE, Kashani MM. A Markov chain-based model for structural vulnerability assessment of corrosion-damaged reinforced concrete bridges. *Philos Trans R Soc A Math Phys Eng Sci*. 2021;379(2203):20200290. https://doi.org/10.1098/rsta.2020.0290
6. Vu KAT, Stewart MG. Structural reliability of concrete bridges including improved chloride-induced corrosion models. *Struct Saf*. 2000; 22(4): 313-333. https://doi.org/10.1016/S0167-4730(00)00018-7

7. Rao AS, Lepech MD, Kiremidjian AS, Sun XY. Simplified structural deterioration model for reinforced concrete bridge piers under cyclic loading 1. *Life-Cycle Struct Syst*. 2019. https://doi.org/10.1201/9781351204590-6

8. Aljawhari K, Gentile R, Freddi F, Galasso C. Effects of ground-motion sequences on fragility and vulnerability of case-study reinforced concrete frames. *Bull Earthq Eng*. 2021;19:6329-6359. https://doi.org/10.1007/s10518-020-01006-8. Published online 2020.

9. Biondini F, Camnasio E, Palermo A. Lifetime seismic performance of concrete bridges exposed to corrosion. *Struct Infrastruct Eng*. 2014;10(7):880-900. https://doi.org/10.1080/15732479.2012.761248

10. Parker M, Steenkamp D. The economic impact of the Canterbury earthquakes. *Reserv Bank New Zeal Bull*. 2012;75:13-25.

11. Jia G, Gardoni P, Trejo D, Mazarei V. Stochastic modeling of deterioration and time-variant performance of reinforced concrete structures under joint effects of earthquakes, corrosion, and ASR. *J Struct Eng*. 2021;147(2):04020314. https://doi.org/10.1061/(asce)st.1943-541x.0002884

12. Panchireddi B, Ghosh J. Cumulative vulnerability assessment of highway bridges considering corrosion deterioration and repeated earthquake events. *Bull Earthq Eng*. 2019;17(3):1603-1638. https://doi.org/10.1007/s10518-018-0509-3

13. Hatzigeorgiou GD, Beskos DE. Inelastic displacement ratios for SDOF structures subjected to repeated earthquakes. *Eng Struct*. 2009;31(11):2744-2755. https://doi.org/10.1016/j.engstruct.2009.07.002

14. Di Sarno L. Effects of multiple earthquakes on inelastic structural response. *Eng Struct*. 2013;56:673-681. https://doi.org/10.1016/j.engstruct.2013.05.041

15. Hatzigeorgiou GD, Liolios AA. Nonlinear behaviour of RC frames under repeated strong ground motions. *Soil Dyn Earthq Eng*. 2010;30(10):1010-1025. https://doi.org/10.1016/j.soildyn.2010.04.013

16. Iervolino I, Giorgio M, Chioccarelli E. Markovian modeling of seismic damage accumulation. *Earthq Eng Struct Dyn*. 2016;45(3):441-461. https://doi.org/10.1002/eqe.2668

17. Ghosh J, Padgett JE. Probabilistic seismic loss assessment of aging bridges using a component-level cost estimation approach. *Earthq Eng Struct Dyn*. 2011;40(15):1743-1761. https://doi.org/10.1002/eqe.1114

18. Panchireddi B, Ghosh J. Probabilistic seismic loss estimation of aging highway bridges subjected to multiple earthquake events. *Struct Infrastruct Eng*. 2021;17(9):1155-1174. https://doi.org/10.1080/15732479.2020.1801765

19. Capacci L, Biondini F, Titi A. Lifetime seismic resilience of aging bridges and road networks. *Struct Infrastruct Eng*. 2020;16(2):266-286. https://doi.org/10.1080/15732479.2019.1653937

20. Decò A, Frangopol DM. Life-cycle risk assessment of spatially distributed aging bridges under seismic and traffic hazards. *Earthq Spectra*. 2013;29(1):127-153. https://doi.org/10.1193/1.4000094

21. Capacci L, Biondini F. Probabilistic life-cycle seismic resilience assessment of aging bridge networks considering infrastructure upgrading. *Struct Infrastruct Eng*. 2020;16(4):659-675. https://doi.org/10.1080/15732479.2020.1716258

22. Shekhar S, Ghosh J, Padgett JE. Seismic life-cycle cost analysis of ageing highway bridges under chloride exposure conditions: modelling and recommendations. *Struct Infrastruct Eng*. 2018;14(7):941-966. https://doi.org/10.1080/15732479.2018.1437639

23. Akiyama M, Frangopol DM, Matsuzaki H. Life-cycle reliability of RC bridge piers under seismic and airborne chloride hazards. *Earthq Eng Struct Dyn*. 2011;40(15):1671-1687. https://doi.org/10.1002/eqe.1108

24. Strauss A, Wendner R, Bergmeister K, Costa C. Numerically and experimentally based reliability assessment of a concrete bridge subjected to chloride-induced deterioration. *J Infrastruct Syst*. 2013;19(2):166–175. https://doi.org/10.1061/(asce)is.1943-555x.0000125

25. Costa C, Figueiredo R, Silva V, Bazzurro P. Application of open tools and datasets to probabilistic modeling of road traffic disruptions due to earthquake damage. *Earthq Eng Struct Dyn*. 2020;49(12):1236–1255. https://doi.org/10.1002/eqe.3288

26. Perdomo C, Abarca A, Monteiro R. Estimation of seismic expected annual losses for multi-span continuous RC bridge portfolios using a component-level approach. *J Earthq Eng*. 2022;26(6):2985-3011. doi:10.1080/13632469.2020.1781710

27. Ancheta TD, Darragh RB, Stewart JP, et al. NGA-West2 database. *Earthq Spectra*. 2014;30(3):989-1005. doi:10.1193/070913EQS197M

28. Galasso C, Kaviani P, Tsioulou A, Zareian F. Validation of ground motion simulations for historical events using skewed bridges. *J Earthq Eng*. 2020;24(10):1652-1674. https://doi.org/10.1080/13632469.2018.1483277

29. Graves R, Jordan TH, Callaghan S, et al. CyberShake: a physics-based seismic hazard model for southern California. *Pure Appl Geophys*. 2011;168(3-4):367-381. https://doi.org/10.1007/s00024-010-0161-6

30. Maechling PJ, Silva F, Callaghan S, Jordan TH. SCEC broadband platform: system architecture and software implementation. *Seismol Res Lett*. 2015;86(1):27-38. https://doi.org/10.1785/0220140125

31. Bradley BA, Pettinga D, Baker JW, Fraser J. Guidance on the utilization of earthquake-induced ground motion simulations in engineering practice. *Earthq Spectra*. 2017;33(3):809-835. doi:10.1193/120216EQS219EP

32. Graves R, Pitarka A. Refinements to the Graves and Pitarka (2010) broadband ground-motion simulation method. *Seismol Res Lett*. 2015;86(1):75-80. https://doi.org/10.1785/0220140101

33. Field EH, Dawson TE, Felzer KR, et al. Uniform California earthquake rupture forecast, version 2 (UCERF 2). *Bull Seismol Soc Am*. 2009;99(4):2053. doi:10.1785/0120080049

34. Fayaz J, Rezaeian S, Zareian F. Evaluation of simulated ground motions using probabilistic seismic demand analysis: cyberShake (ver. 15.12) simulations for Ordinary Standard Bridges. *Soil Dyn Earthq Eng*. 2021;141:106533. https://doi.org/10.1016/j.soildyn.2020.106533

35. Baker JW, Rezaeian S, Goulet CA, Luco N, Teng G. A subset of CyberShake ground-motion time series for response-history analysis. Earthq Spectra. 2021;37(2):1162-1176. doi:10.1177/8755293020981970

36. Fayaz J, Azar S, Dabaghi M, Zareian F. Methodology for validation of simulated ground motions for seismic response assessment: application to cybershake source-based ground motions. *Bull Seismol Soc Am*. 2021;111(1):226-241. https://doi.org/10.1785/0120200240

37. Kohrangi M, Vamvatsikos D, Bazzurro P. Site dependence and record selection schemes for building fragility and regional loss assessment. *Earthq Eng Struct Dyn*. 2017;46(10):1625-1643. https://doi.org/10.1002/eqe.2873

38. Papadopoulos AN, Kohrangi M, Bazzurro P. Mainshock-consistent ground motion record selection for aftershock sequences. *Earthq Eng Struct Dyn*. 2020;49(8):754-771. https://doi.org/10.1002/eqe.3263

39. Bradley BA. A ground motion selection algorithm based on the generalized conditional intensity measure approach. *Soil Dyn Earthq Eng*. 2012;40:48-61. https://doi.org/10.1016/j.soildyn.2012.04.007

40. Kazantzi AK, Vamvatsikos D. Intensity measure selection for vulnerability studies of building classes. *Earthq Eng Struct Dyn*. 2015;44(15):2677-2694. https://doi.org/10.1002/eqe.2603

41. Eads L, Miranda E, Lignos DG. Average spectral acceleration as an intensity measure for collapse risk assessment. *Earthq Eng Struct Dyn*. 2015;44(12):2057-2073. https://doi.org/10.1002/eqe.2575

42. Jawad F, Mayssa D, Farzin Z. Utilization of site-based simulated ground motions for hazard-targeted seismic demand estimation: Application for ordinary bridges in Southern California. *J Bridg Eng*. 2020;25(11):4020097. doi:10.1061/(ASCE)BE.1943-5592.0001634

43. Wibowo H, Sritharan S. Effects of vertical ground acceleration on the seismic moment demand of bridge superstructure connections. *Eng Struct*. 2022;253:113820. https://doi.org/10.1016/J.ENGSTRUCT.2021.113820

44. Kaviani P, Zareian F, Taciroglu E. Seismic behavior of reinforced concrete bridges with skew-angled seat-type abutments. *Eng Struct*. 2012;45:137-150. https://doi.org/10.1016/j.engstruct.2012.06.013

45. Boore DM. Orientation-independent, nongeometric-mean measures of seismic intensity from two horizontal components of motion. *Bull Seismol Soc Am*. 2010;100(4):1830-1835. https://doi.org/10.1785/0120090400

46. O'Reilly GJ. Seismic intensity measures for risk assessment of bridges. *Bull Earthq Eng*. 2021;19(9):3671-3699. https://doi.org/10.1007/s10518-021-01114-z

47. Iacoletti S, Cremen G, Galasso C. Advancements in multi-rupture time-dependent seismic hazard modeling, including fault interaction. *Earth-Science Rev*. 2021;220:103650. https://doi.org/10.1016/j.earscirev.2021.103650

48. Zhu M, McKenna F, Scott MH. OpenSeesPy: python library for the OpenSees finite element framework. *SoftwareX*. 2018;7:6-11. https://doi.org/10.1016/j.softx.2017.10.009

49. Omrani R, Mobasher B, Sheikhakbari S, Zareian F, Taciroglu E. Variability in the predicted seismic performance of a typical seat-type California bridge due to epistemic uncertainties in its abutment backfill and shear-key models. *Eng Struct*. 2017;148:718-738. https://doi.org/10.1016/j.engstruct.2017.07.018

50. Xiang Y, Fayaz J, Zareian F. Validation of Caltrans ordinary bridge modeling approach using Bayesian state and parameter estimation method. California Strong Motion Instrumentation Program (CSMIP); 2020.

51. Caltrans. *Seismic Design Criteria. Version 1.7*. Sacramento, CA: California Department of Transportation; 2013.

52. Kaviani P, Zareian F, Tacifoglu E. *Performance-Based Seismic Assessment of Skewed Bridges*. Pacific Earthquake Engineering Research Center (PEER); 2014.

53. Kottari A, Design and Capacity Assessment of External Shear Keys in Bridge Abutments. Published online 2016.

54. Choi E. Seismic analysis and retrofit of Mid-America bridges. Atlanta (G.A.): Department of Civil and Environmental Engineering, Georgia Institute of Technology, Ph.D. Thesis; 2002.

55. Shamsabadi A, Kapuskar M. Nonlinear soil-abutment-foundation- Structure interaction analysis of skewed bridges subjected to near-field ground motions. *Transp Res Rec*. 2010;2202:192-205. https://doi.org/10.3141/2202-23

56. Ramanathan K. *Next Generation Seismic Fragility Curves for California Bridges Incorporating the Evolution in Seismic Design Philosophy*. Atlanta (G.A.): Department of Civil and Environmental Engineering, Georgia Institute of Technology, Ph.D. Thesis; 2012.

57. Claisse PA. *Corrosion of Steel in Concrete – Understanding, Investigation and Repair*. 2nd ed. Broomf J P, Taylor Fr London; 2008. 978-0-4153(3404-4).

58. Kashani MM, Crewe AJ, Alexander NA. Nonlinear stress-strain behaviour of corrosion-damaged reinforcing bars including inelastic buckling. *Eng Struct*. 2013;48:417-429. https://doi.org/10.1016/j.engstruct.2012.09.034

59. Martin JL. *Hydro-Environmental Analysis: Freshwater Environments* (1st Ed.). CRC Press; 2013. doi:10.1201/b16108

60. Hanjari KZ, Kettil P, Lundgren K. Analysis of mechanical behavior of corroded reinforced concrete structures. *ACI Struct J*. 2011;108(5):532-541. 10.14359/51683210

61. Stewart MG. Spatial variability of pitting corrosion and its influence on structural fragility and reliability of RC beams in flexure. *Struct Saf*. 2004;26(4):453-470. https://doi.org/10.1016/j.strusafe.2004.03.002

62. Kashani MM, Crewe AJ, Alexander NA. Use of a 3D optical measurement technique for stochastic corrosion pattern analysis of reinforcing bars subjected to accelerated corrosion. *Corros Sci*. 2013;73:208-221. https://doi.org/10.1016/j.corsci.2013.03.037

63. Dizaj EA, Madandoust R, Kashani MM. Probabilistic seismic vulnerability analysis of corroded reinforced concrete frames including spatial variability of pitting corrosion. *Soil Dyn Earthq Eng*. 2018;114:97-112. https://doi.org/10.1016/j.soildyn.2018.07.013

64. Srivaranun S, Akiyama M, Bocchini P, et al. Effect of the interaction of corrosion pits among multiple tensile rebars on the reliability of RC structures: experimental and numerical investigation. *Struct Saf*. 2021;93:102115. https://doi.org/10.1016/j.strusafe.2021.102115

65. Coronelli P, Gambarova D. Structural assessment of corroded reinforced concrete beams: Modeling guidelines. *J Struct Eng*. 2004;130(8):1214-1224. doi:10.1061/(ASCE)0733-9445(2004)130:8(1214)

66. Vecchio FJ, Collins MP. Modified compression-field theory for reinforced concrete elements subjected to shear. *J Am Concr Inst*. 1986;83(2):219-231. 10.14359/10416

67. Molina FJ, Alonso C, Andrade C. Cover cracking as a function of rebar corrosion: part 2-Numerical model. *Mater Struct*. 1993;26(9):532-548. https://doi.org/10.1007/BF02472864

68. Mander JB, Priestley MJN, Park R. Theoretical stress–strain model for confined concrete. *J Struct Eng*. 1988;114(8):1804-1826. doi:10.1061/(ASCE)0733-9445(1988)114:8(1804)

69. Zhang G, Cao X, Fu Q. Literature review on experiment study on RC element with corroded rebar. In: Xia J, ed. Sustainable Buildings and Structures - Proceedings of the 1st International Conference on Sustainable Buildings and Structures (ICSBS) (1st Ed.). CRC Press; 2015:8. https://doi.org/10.1201/b19239-13

70. Du YG, Clarkt LA, Chan AHC. Effect of corrosion on ductility of reinforcing bars. *Mag Concr Res*. 2005;57(7):407-419. https://doi.org/10.1680/macr.2005.57.7.407

71. Du YG, Clark LA, Chan AHC. Residual capacity of corroded reinforcing bars. *Mag Concr Res*. 2005;57(3):135-147. https://doi.org/10.1680/macr.2005.57.3.135

72. Andisheh K, Scott A, Palermo A. Seismic behavior of corroded RC bridges: Review and research gaps. *Int J Corros*. 2016;2016(2):1-22. doi:10.1155/2016/3075184

73. Apostolopoulos CA, Papadakis VG. Consequences of steel corrosion on the ductility properties of reinforcement bar. *Constr Build Mater*. 2008;22(12):2316-2324. https://doi.org/10.1016/j.conbuildmat.2007.10.006

74. Biondini F, Vergani M. Deteriorating beam finite element for nonlinear analysis of concrete structures under corrosion. *Struct Infrastruct Eng*. 2015;11(4):519-532. https://doi.org/10.1080/15732479.2014.951863

75. Kashani MM, Lowes LN, Crewe AJ, Alexander NA. Phenomenological hysteretic model for corroded reinforcing bars including inelastic buckling and low-cycle fatigue degradation. *Comput Struct*. 2015;156:58-71. https://doi.org/10.1016/j.compstruc.2015.04.005

76. Wang X, Liu X. Modeling bond strength of corroded reinforcement without stirrups. *Cem Concr Res*. 2004;34(8):1331-1339. https://doi.org/10.1016/j.cemconres.2003.12.028

77. Priestley MJN, Seible F, Calvi GM. *Seismic Design and Retrofit of Bridges* (1st Ed.). John Wiley & Sons, Inc.; 1996. doi:10.1002/9780470172858

78. Hwang H, Liu JB, Chiu YH. Seismic Fragility Analysis of Highway Bridges. *9th ASCE Spec Conf Probabilistic Mech Struct Reliab*. 2001.

79. Mander JB, Priestley MJN, Park R. Observed stress-strain behavior of confined concrete. *J Struct Eng*. 1988;114(8). https://doi.org/10.1061/(asce)0733-9445(1988)114:8(1827)

80. Paulay T, Priestly MJN. *Seismic Design of Reinforced Concrete and Masonry Buildings* (1st Ed.). John Wiley & Sons, Inc.; 1992. doi:10.1002/9780470172841

81. Ramanathan K, Padgett JE, DesRoches R. Temporal evolution of seismic fragility curves for concrete box-girder bridges in California. *Eng Struct*. 2015;97:29-46. https://doi.org/10.1016/j.engstruct.2015.03.069

82. Ghosh J, Sood P. Consideration of time-evolving capacity distributions and improved degradation models for seismic fragility assessment of aging highway bridges. *Reliab Eng Syst Saf*. 2016;154:197-218. https://doi.org/10.1016/j.ress.2016.06.001

83. American Society of Civil Engineers. *ASCE Standard, ASCE/SEI, 41-17, Seismic Evaluation and Retrofit of Existing Buildings*; 2017.

84. Behzad Z, E PJ, Gholamreza GA. Fragility assessment for seismically retrofitted skewed reinforced concrete box girder bridges. *J Perform Constr Facil*. 2015;29(2):4014043. doi:10.1061/(ASCE)CF.1943-5509.0000502

85. FEMA. HAZUS-MH MR4 technical manual, multi-hazard loss estimation methodology earthquake model. FEMA 366, Washington, DC; 2003.

86. Gentile R, Galasso C. Hysteretic energy-based state-dependent fragility for ground-motion sequences. *Earthq Eng Struct Dyn*. 2021;50(4):1187-1203. doi:10.1002/eqe.3387

87. Applied Technology Council (ATC). Seismic performance assessment of buildings volume 1 – methodology. FEMA P-58-1. *Fed Emerg Manag Agency*. 2012;1(August):278.

88. Jalayer F, Ebrahimian H, Miano A, Manfredi G, Sezen H. Analytical fragility assessment using unscaled ground motion records. *Earthq Eng Struct Dyn*. 2017;46(15):2639-2663. https://doi.org/10.1002/eqe.2922

89. Baker JW. Efficient analytical fragility function fitting using dynamic structural analysis. Earthq Spectra. 2015;31(1):579-599. doi:10.1193/021113EQS025M

90. Padgett JE, Desroches R, Nilsson E. Regional seismic risk assessment of bridge network in Charleston, South Carolina. *J Earthq Eng*. 2010;14(6):918-933. https://doi.org/10.1080/13632460903447766